Cell Reports

Article

Early precursor-derived pituitary gland tissue-resident macrophages play a pivotal role in modulating hormonal balance

Graphical abstract

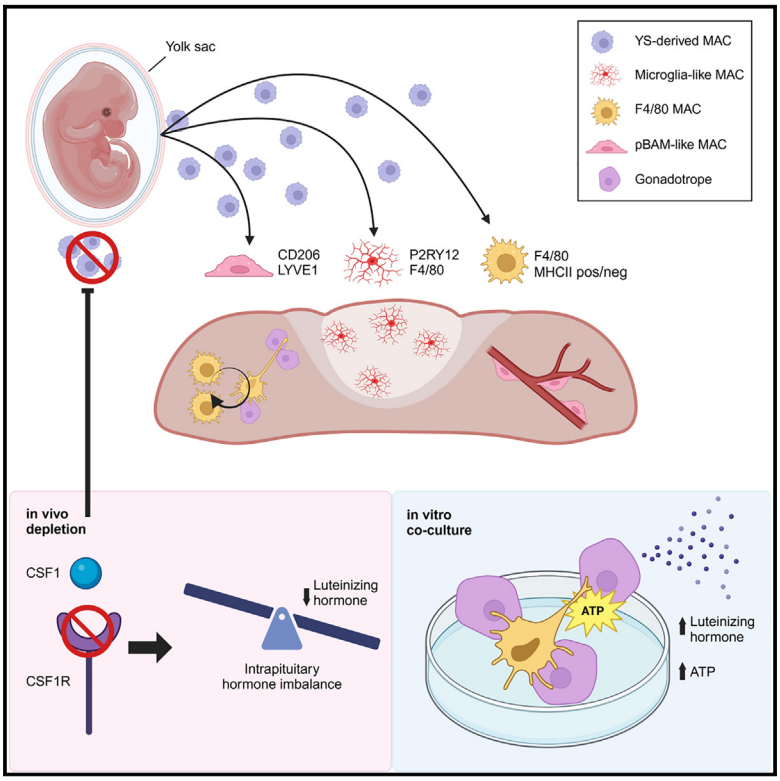

Authors

Henna Lehtonen, Heli Jokela, Julian Hofmann, ..., Marko Salmi, Heidi Gerke, Pia Rantakari

Correspondence

pia.rantakari@utu.fi

In brief

The pituitary gland hosts specialized macrophages (pitMØs) that regulate immune-endocrine interactions. Lehtonen et al. reveal the spatial heterogeneity and yolk sac origin of pitMØs. Microglia-like pitMØs enrich the posterior pituitary, while anterior pitMØs interact with hormone-secreting cells. Macrophages modulate intrapituitary hormonal balance, advancing immune-endocrine research.

Highlights

- Pituitary gland macrophages originate from early yolk sac progenitors
- Microglia-like pitMØs localize in the posterior, while others home in the anterior pituitary
- Macrophage depletion unveils their role in regulating intrapituitary hormonal balance

Lehtonen et al., 2025, Cell Reports *44*, 115227
February 25, 2025
https://doi.org/10.1016/j.celrep.2024.115227

CellPress

Cell Reports

CellPress
OPEN ACCESS

Article

Early precursor-derived pituitary gland tissue-resident macrophages play a pivotal role in modulating hormonal balance

Henna Lehtonen,[1,2,3,11] Heli Jokela,[1,2,3,11] Julian Hofmann,[1,2,3] Lauriina Tola,[1,2,3] Arfa Mehmood,[2,3] Florent Ginhoux,[4,5,6,7,8] Burkhard Becher,[9] Melanie Greter,[9] Gennady G. Yegutkin,[3,10] Marko Salmi,[2,3,10] Heidi Gerke,[1,2,3] and Pia Rantakari[1,2,3,12,*]

[1]Turku Bioscience Centre, University of Turku and Åbo Akademi University, 20520 Turku, Finland
[2]Institute of Biomedicine, University of Turku, 20520 Turku, Finland
[3]InFLAMES Research Flagship Center, University of Turku, 20520 Turku, Finland
[4]Shanghai Institute of Immunology, Shanghai Jiao Tong University School of Medicine, Shanghai 200025, China
[5]Singapore Immunology Network, Agency for Science, Technology and Research, Singapore 138648, Singapore
[6]INSERM U1015, Gustave Roussy Cancer Campus, Villejuif 94800, France
[7]Translational Immunology Institute, SingHealth Duke-NUS, Singapore 169856, Singapore
[8]Department of Microbiology and Immunology, Yong Loo Lin School of Medicine, National University of Singapore, Singapore, Singapore
[9]Institute of Experimental Immunology, University of Zürich, 8057 Zurich, Switzerland
[10]MediCity Research Laboratory, University of Turku, 20520 Turku, Finland
[11]These authors contributed equally
[12]Lead contact
*Correspondence: pia.rantakari@utu.fi
https://doi.org/10.1016/j.celrep.2024.115227

SUMMARY

The pituitary gland is the central endocrine regulatory organ producing and releasing hormones that coordinate major body functions. The physical location of the pituitary gland at the base of the brain, though outside the protective blood-brain barrier, leads to an unexplored special immune environment. Using single-cell transcriptomics, fate mapping, and imaging, we characterize pituitary-resident macrophages (pitMØs), revealing their heterogeneity and spatial specialization. Microglia-like macrophages (ml-MACs) are enriched in the posterior pituitary, while other pitMØs in the anterior pituitary exhibit close interactions with hormone-secreting cells. Importantly, all pitMØs originate from early yolk sac progenitors and maintain themselves through self-renewal, independent of bone marrow-derived monocytes. Macrophage depletion experiments unveil the role of macrophages in regulating intrapituitary hormonal balance through extracellular ATP-mediated intercellular signaling. Altogether, these findings provide information on pituitary gland macrophages and advance our understanding of immune-endocrine system crosstalk.

INTRODUCTION

The pituitary gland is a central endocrine organ located underneath the brain. Being connected to the hypothalamus via a stalk, including blood vessels and nerves, the pituitary gland acts as a signal mediator between the hypothalamus and peripheral organs. The function of the pituitary gland is to produce and release hormones and, thus, coordinate several physiological functions such as growth, reproduction, and stress response.[1–3] The pituitary gland comprises two ectodermal structures.[1,4] The neural ectoderm gives rise to the posterior lobe, responsible for storing and secreting arginine vasopressin (AVP) and oxytocin (OXT), produced by the hypothalamus.[5] The surface ectoderm, forming Rathke's pouch, gives rise to the anterior and intermediate lobes. The intermediate lobe consists of melanotrophs producing melanocyte-stimulating hormone, while the anterior lobe contains five specialized endocrine cell types secreting various hormones, along with non-endocrine cells such as folliculostellate (FS) cells, vascular endothelial cells, and immune cells.[3,4,6]

Macrophages are critical regulators of tissue homeostasis.[7–9] Tissue-resident macrophages generally originate from embryonic precursors (yolk sac and/or fetal liver) and are maintained locally through self-renewal.[10,11] Under homeostatic conditions, each adult organ has its own ontogenetically and functionally distinct macrophage pool controlling tissue-specific and niche-specific functions.[10,12–18] Diverse roles played by macrophages have also been described in endocrine organs.[19–26] Macrophages in pancreatic islets are vital players in metabolic inflammation, underlining the development of insulin resistance.[19] In the ovaries, they play an essential role in ovarian folliculogenesis and ovulation,[20,27] and in the male reproductive tract, they regulate vascularization and spermatogenesis.[21,28,29]

In the pituitary gland, macrophages form the foremost immune cell population.[30,31] However, the origin, features, or their relationship to pituitary gland function in homeostasis or

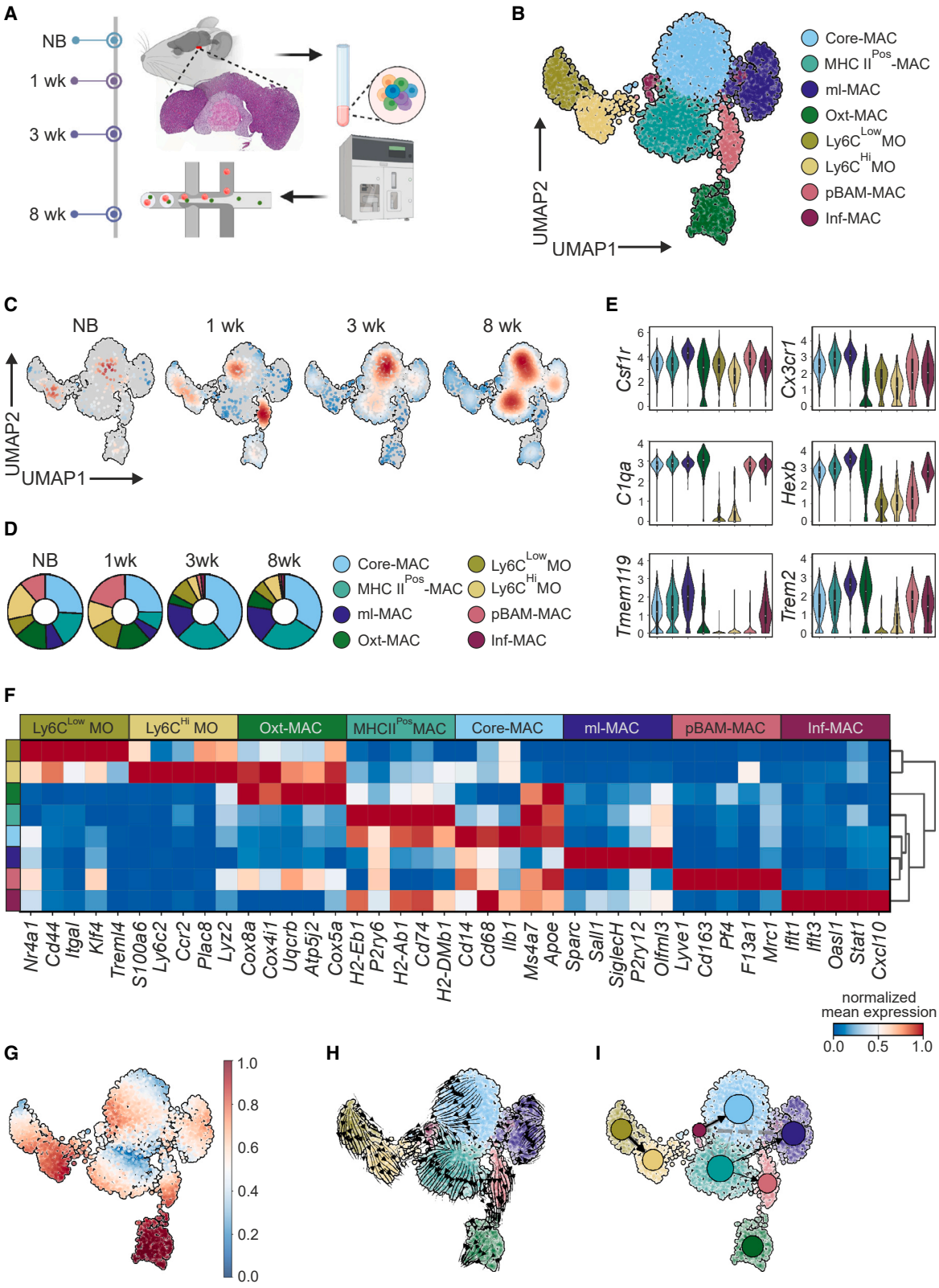

(legend on next page)

pathological conditions are not understood. Herein, we constructed a high-density transcriptional map elucidating the intricacies of pituitary gland macrophages (pitMØs) and unveiled their developmental kinetics and distinctive characteristics, shedding light on the nuanced dynamics of pitMØ development. Within pitMØs, we identified microglia-like macrophages in the posterior lobe and vascular-associated macrophages in the anterior lobe of the pituitary gland. Furthermore, we revealed that the pitMØs originate from the early yolk sac precursors and relies on proliferation for self-maintenance. Macrophage depletion revealed a role for macrophages in the homeostatic development of the pituitary gland. By modulating extracellular ATP availability and, consequently, calcium signaling within the gland, depletion led to abnormal pituitary hormone levels. Altogether, these findings offer new insights into the immune landscape of the pituitary gland, highlighting the role of macrophages in maintaining hormonal balance.

RESULTS

At a steady state, the pituitary gland hosts transcriptionally distinct macrophage subsets

To gain a comprehensive view of macrophage subsets that reside within the developing homeostatic pituitary gland, we collected the whole pituitary glands from newborn (NB) to adult (8 weeks of age) wild-type (WT) mice, isolated CD45^{+} leukocytes by fluorescent-activated cell sorting (FACS) before single-cell sequencing (scRNA-seq; Figure 1A). scRNA-seq analyses revealed the complex immune environment in the developing pituitary gland (Figures S1A-S1C). We further sub-clustered macrophage populations expressing canonical markers (*Fcgr1*, *Adgre1*, *Cd68*) and monocyte populations with *Itgam* and either *Ly6c2* or *Nr4a1*. Low-quality and mixed-cell clusters were excluded (Figures S1B, S1D, and S1E). The subclustering allowed for a more detailed assessment of these cells and identified six macrophage and two monocyte clusters (Figure 1B). Cluster frequencies showed dynamic progression and fluctuation, with a dramatic postnatal increase in total pitMØs (Figures 1C, 1D, and S1F).

All macrophage clusters were uniformly expressing *Csf1r*, *Cx3cr1*, and *C1qa*, and the majority were also highly expressing *Hexb*, *Tmem119*, and *Trem2*, typical markers for microglia (Figure 1E). Core-MAC and MHC II^{Pos}-MAC subclusters were predominant in all stages and exhibited similar overlapping transcriptomic profiles (Figures 1D, 1F, S1F, and S1G). Core-MACs mainly expressed common macrophage markers (e.g., *Cd14*, *Cd86*, and *Il1b*; Figure 1F and Table S1), whereas MHC II^{Pos}-MACs showed increased expression of immune response activation and antigen presentation genes such as *H2-Eb1*, *P2ry6*, *H2-Ab1*, and *Cd74* (Figure 1F and Table S1). Interstingly, ml-MAC macrophages were enriched in microglia signature genes such as *Sall1*, *P2ry12*, and *Nav3*[32–35] and expressed higher levels of *Mertk* than other macrophages in the pituitary gland (Figure 1F and Table S1). On the other hand, pBAM-MACs were expressing a prototypical BAM signature gene such as *Lyve1*, *Mrc1*, and *Stab1*[13,35,36] (Figure 1F and Table S1). The abundance of pBAM-MAC cells peaked at 1 week of age, from where it diminished toward adulthood almost entirely (Figures 1C, 1D, and S1F). Oxt-MACs had a relatively high enrichment of genes related to oxidative phosphorylation (e.g., *Cox8a*, *Cox4i1*, and *Cox6b1*; Figure 1F and Table S1) and showed increased expression of genes involved in ribosomal biogenesis and protein synthesis in activated macrophages (Table S1). The small Inf-MAC cluster appeared after 1 week of age and expressed genes related to response to interferon beta and monocyte differentiation (Figures 1C and 1F and Table S1). The proportion or total Inf-MAC cell number did not markedly increase between juvenile and adult animals (Figures 1D and S1F). We furthermore observed that Core-MACs, ml-MACs, pBAM-MACs, and Inf-MACs were also characterized by a high expression of immediate-early genes (e.g., *Jun*, *Fos*, and *Klf6*) encoding transcription factors that may define transcriptionally active cells (Figure S1H and Table S1). Noteworthy was that *H2-Ab1* (MHC II) expression increased in all the other macrophage populations except ml-MAC as the animals aged (Figure S1I). Two clusters were enriched with typical monocyte markers (Figure 1F). Ly6C^{Hi}MOs expressed classical monocyte markers, such as *S100a6*, *Ly6c2*, and *Ccr2*. Ly6C^{Low}MOs showed the upregulation of *Nr4a1* and *Itgal*, markers used to identify non-classical monocytes (Figure 1F and Table S1).

To examine potential developmental trajectories of the monocyte/macrophage subtypes, we next applied CytoTRACE[37] to predict cell lineage differentiation states of clusters. Pseudotime differentiation trajectory analysis showed that Oxt-MAC cells were the most differentiated, while Core-MACs and the MHC II^{Pos}-MACs were the least differentiated. Interestingly, pBAM-MACs were in intermediate transitions between the differentiation stages (Figure 1G). The directed transition matrix on a uniform manifold approximation and projection (UMAP) representation with original macrophage/monocyte cluster annotations further suggested that Core-MACs and MHC II^{Pos}-MACs likely serve as origin of pBAM-MACs, which would eventually differentiate toward Oxt-MAC cells

Figure 1. At a steady state, the pituitary gland hosts macrophage and monocyte subsets that exhibit distinct transcriptional variability

(A) Workflow of scRNA-seq. Created with BioRender.com.

(B) Uniform manifold approximation and projection (UMAP) plot of mouse pitMØs and monocytes colored by the cluster.

(C) UMAP plots highlighting the cell embedding across timepoints. Color intensity represents cell density from low (blue) to high (red).

(D) Donut charts present the cell frequency of pitMØs and monocytes in the pituitary gland.

(E) Violin plots showing expression of selected genes in pitMØ and monocyte clusters.

(F) Heatmap of single-cell expression of selected DEGs in pitMØ and monocyte clusters. The color indicates the expression level from low (blue) to high (red).

(G) CytoTRACE-predicted transcriptional dynamics of pitMØs and monocytes on the UMAP. The color code indicates the computed cell differentiation level from less (blue) to highly differentiated (red).

(H) Differentiation velocity field of pitMØs and monocytes on the UMAP. Arrow lines indicate putative developmental differentiation trajectories.

(I) PAGA analysis with pseudotime-directed edges of pitMØs and monocytes projected on the UMAP with node connectivities (dashed) and directed transitions (solid/arrows).

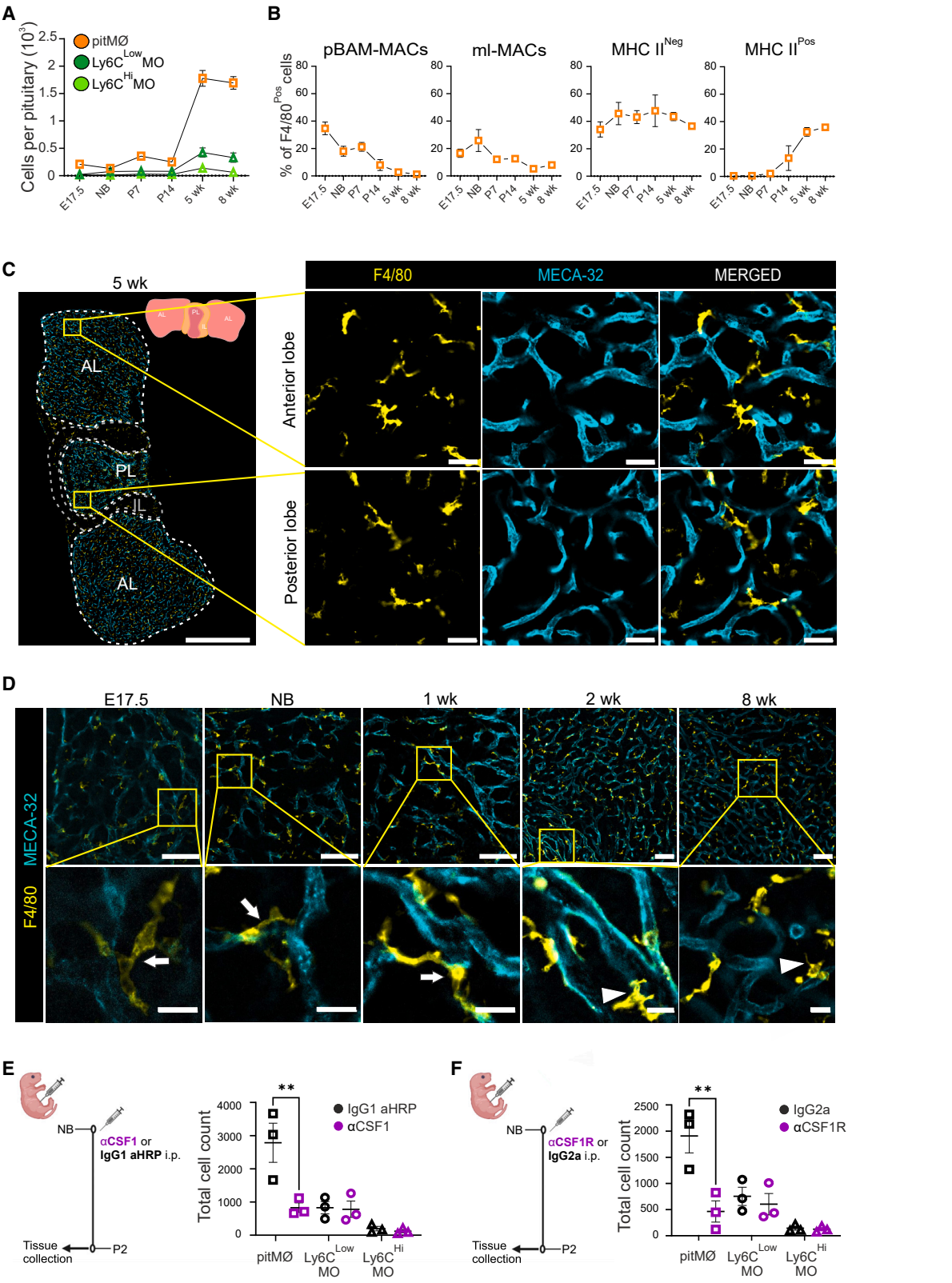

(legend on next page)

(Figure 1H). Interestingly, the ml-MACs appeared to be an independent and distinct cellular state. No clear transition was evident from the other macrophage or monocyte subpopulations to the ml-MACs cells, and the transition matrix did not point toward any other clusters from the ml-MACs (Figure 1H). Monocyte subpopulations (Ly6C^{Hi}MO and Ly6C^{Low}MO) emerged as distinct entities outside the central trajectory and intriguingly, did not exhibit directional vectors toward the macrophage lineages (Figure 1H). Partition-based graph abstraction (PAGA)[38] analysis recapitulated the central trajectory trends and indicated pBAM-MACs as an intermediate state, connecting Core-MACs and MHC II^{Pos}-MACs to Oxt-MACs. Ly6C^{Hi}MO and Ly6C^{Low}MO populations emerged as clear outliers, as they deviated significantly from the central trajectory, consistent with transition matrix analyses (Figures 1H and 1I). Collectively, our data reveal the coexistence of multiple diverse macrophage populations, which numbers increased with age. Moreover, data analyses suggest that the monocyte precursors may not considerably contribute to the development of pitMØs.

Tissue growth induces modification in the phenotype of pituitary gland macrophages

Next, we used the transcriptomic information as a base to distinguish macrophages using flow cytometry. Expression of CD11b, Ly6C, and F4/80 allowed the resolution of total macrophages (F4/80^{Pos}Ly6C^{Neg}; pitMØ) and two monocyte subsets, presenting both tissue-resident and possible blood-circulating monocytes (Figure 2A, and S2A-S2B for gating strategy). The cell numbers of pitMØs increased manifold when the growth of the pituitary gland is most significant, between the ages of P14 and 5 weeks. However, both monocyte subsets, the Ly6C^{Hi}MO (Ly6C^{Hi}CX3CR1^{Low}; classical monocytes) and Ly6C^{Low}MO (Ly6C^{Low}CX3CR1^{Hi}; non-classical monocytes) stayed at constant low cell amount and frequency levels throughout all time points studied (Figure 2A and S2C). The pitMØs, which also expressed common macrophage markers CD64 and CX3CR1, were observed throughout various stages of development (Figure S2D).

In line with the scRNA-seq data, we subdivided the pitMØs by flow cytometry into the pBAM-MAC population, identified by CD206 expression, and the ml-MAC subpopulation, marked by P2RY12 expression (Figures S2A and S2B). The remaining macrophages from transcriptomic analysis (Core-MACs, MHC II^{Pos}-MACs, Oxt-MACs, and Inf-MACs) could not be individually distinguished by flow cytometry. However, at the transcriptomics level, these cells could be classified based on MHC II expression (Figure S1I). Therefore, in flow cytometry analyses, we collectively refer to them as either MHC II^{Pos}-MAC or MHC II^{Neg}-MAC (Figures S2A and S2B). At E17.5, the CD206-positive pBAM-MACs formed around 35% of pitMØs, but diminished after 1 week of age in the pituitary gland (Figure 2B), as observed in scRNA-seq data (Figure 1D and S1E). Likewise, the P2RY12-positive ml-MACs were already present in the E17.5 pituitary gland and remained detectable over time (Figure 2B). The expression of MHC II was not found during the early development of the pituitary gland (E17.5 and NB) but increased significantly in the postnatal pituitary gland (Figure 2B). Interestingly, the disappearance of pBAMs and the appearance of MHC II^{Pos}-MACs were evident during the same period from 1 to 2 weeks (Figures S1A–S1C). We observed that pitMØs were scattered throughout the pituitary gland stroma, both in anterior and posterior lobes, but, as shown previously,[31,39] were not frequent in the intermediate lobe of the pituitary gland (Figures 2C, S2E, and S2F). At early time points (E17.5, NB, and 1 week), many macrophages exhibited a more rounded phenotype, whereas in the pituitaries of 2- to 8-week-old mice, macrophages presented the typical morphology of mature phagocytes with multiple dendrites (Figure 2D).

The colony-stimulating factor 1 receptor (CSF1R, also known as M-CSFR or CD115) is essential for macrophage development, differentiation, and survival.[40,41] The receptor has two ligands, colony-stimulating factor 1 (CSF1) and interleukin (IL)-34.[42] To assess if CSF1 or IL-34 is required to maintain the pitMØs, we first used IL-34-deficient mice.[43] Although IL-34 was expressed in the anterior pituitary gland (Figure S2G), the pitMØs were present at normal numbers in IL-34-deficient mice (Figure S2H). Single injection of neutralizing antibody αCSF1 antibody (clone 5A1), or a function-blocking antibody αCSF1R (clone AFS98) for NB mice both significantly reduced pitMØs within 48 h of treatment (Figures 2E and 2F), with equal depletion across

Figure 2. Development modifies the phenotype of CSF1R-dependent pituitary gland macrophages

(A) The cell amount of pitMØ, Ly6C^{Low}MO, and Ly6C^{Hi}MO cells in the WT pituitary gland at indicated timepoints. The quantitative data are mean ± SEM. Each dot represents data from mice pooled together: E17.5 (n = 8–12 mice/pool), NB (n = 7–11 mice/pool), P7 (n = 4–6 mice/pool), P14 (n = 2–5 mice/pool), and from individual mice at 5 weeks (*n* = 15 mice) and 8 weeks (*n* = 13 mice). Data from six to eight independent experiments.

(B) Frequency of pBAMs, ml-MACs, MHC II^{Neg}, and MHC II^{Pos} cells in F4/80^{Pos} cells in WT pituitary gland at indicated timepoints. The quantitative data are mean ± SEM. Each dot represents data from mice pooled together: E17.5 (*n* = 9–12 mice/pool), NB (*n* = 8–9 mice/pool), P7 (*n* = 4–6 mice/pool), P14 (*n* = 4–5 mice/pool), and from individual mice at 5 weeks (*n* = 8 mice) and 8 weeks (*n* = 9 mice). Data from three to four independent experiments.

(C) Whole-mount immunofluorescence with F4/80 and endothelial marker, MECA-32, from WT pituitary gland of a 5-week-old mouse. Inserts are higher magnifications from the boxed anterior lobe (AL) and posterior lobe (PL) areas. Overview image scale is 500 μm and inserts, 20 μm. Representative images from three independent experiments. IL, intermediate lobe.

(D) Whole-mount immunofluorescence with F4/80 and MECA-32, from WT pituitary glands of E17.5, NB, 1-, 2-, and 8-week-old mice. Inserts are higher magnifications from the boxed areas. Arrows indicate a more rounded phenotype and arrowheads indicate morphology of mature phagocytes of 2- to 8-week-old mice. Overview image scales are 50 μm and inserts, 10 μm. Representative images from three or fewer independent experiments.

(E) Experimental outline for treating NB WT mice with neutralizing CSF1 antibody or control IgG at NB. The cell amount of pitMØ, Ly6C^{Low}MO, and Ly6C^{Hi}MO cells in the WT mouse at postnatal day (P) 2 after neutralizing CSF1 antibody or control IgG treatment. The quantitative data are mean ± SEM. Each dot represents data from mice pooled together: NB (n = 9–10 mice/pool). Data from five independent experiments.

(F) Experimental outline for treating NB WT mice with blocking CSF1R antibody or control IgG. The cell amount of pitMØ, Ly6C^{Low}MO, and Ly6C^{Hi}MO cells in the WT mouse at P2 after blocking CSF1R antibody or control IgG treatment. The quantitative data are mean ± SEM. Each dot represents data from mice pooled together: NB (*n* = 7–11 mice/pool). Data from five independent experiments.

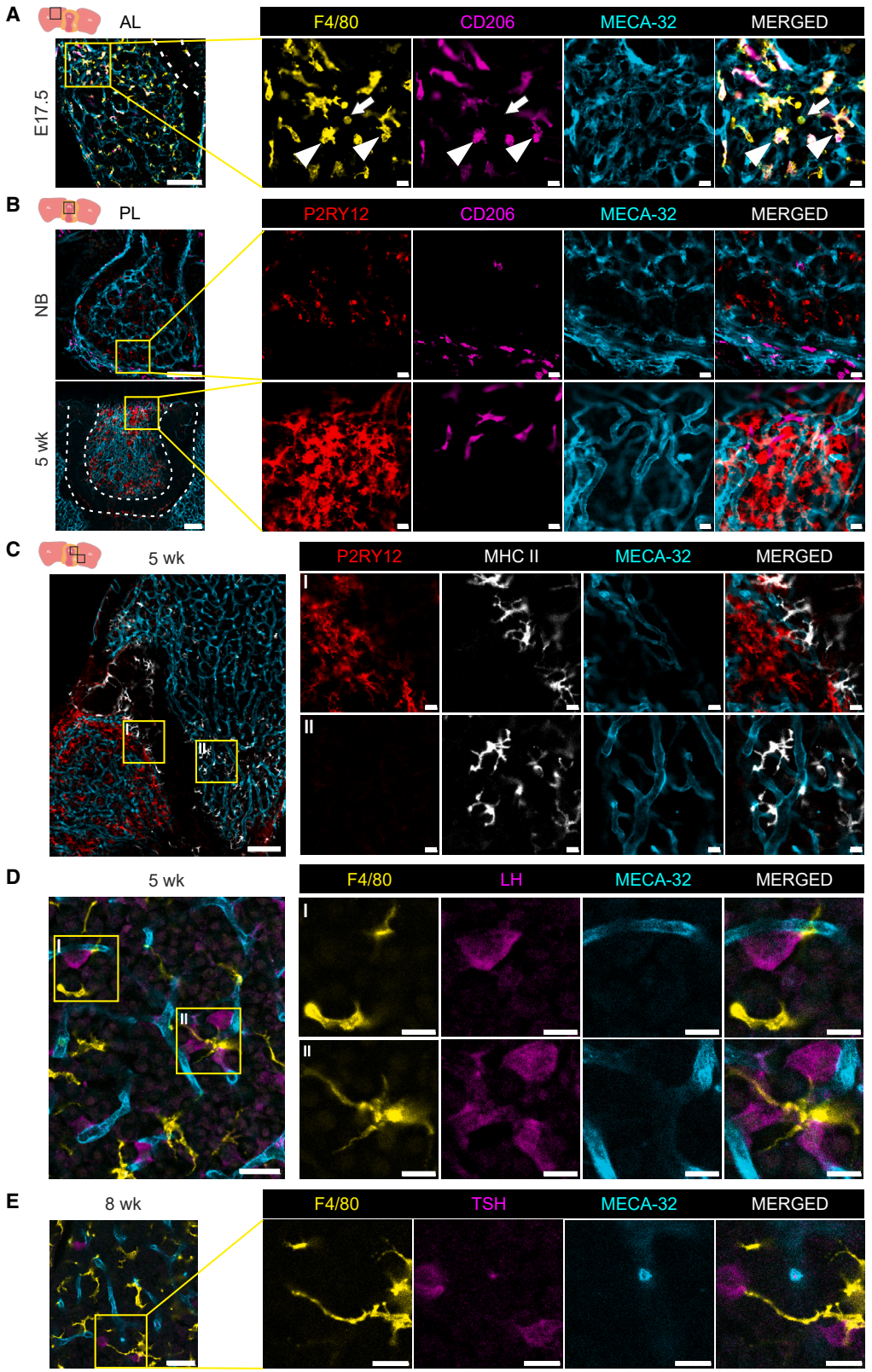

(legend on next page)

macrophage subpopulations (Figure S2I). However, monocyte subsets, Ly6C^{Hi}MO and Ly6C^{Low}MO, were unaffected by αCSF1 and αCSF1R antibody injections (Figures 2E and 2F). Hence, the result confirmed that CSF1R signaling via CSF1 is critical for the homeostasis of pitMØs.

The pituitary gland macrophages are located in distinct spatial niches and interact with endocrine cells

We next examined whether different subpopulations of pitMØs have a specific microanatomical niche in the pituitary gland. In the developing pituitary gland, CD206^{Pos} pBAM-MACs, which also expressed LYVE-1, were predominantly located in the anterior pituitary gland (Figures 3A, S3A, and S3B). The pBAM-MAC cells were closely mingling with blood vessels (Figures 3A, S3A, and S3B), which aligns with previous studies.[13,36] Similar to flow cytometry results, only a few CD206-expressing pBAM-MACs were found in the pituitary gland of the older animals and the few remaining pBAM-MACs were not located in the anterior pituitary gland but in the stalk area, connecting the pituitary gland to the hypothalamus (Figure 3B). MHC II^{Pos}-MACs were only detectable in the anterior pituitary gland of 2-week-old and older mice (Figures 2B and 3C) except for a small number of MHC II-positive cells that resemble the characteristics of macrophages on the boundary of the intermediate lobe (Figure 3C). Notably, the ml-MACs, positive for P2RY12 and F4/80, were solely localized in the stroma of the posterior lobe (Figures 3B, 3C, S3C, and S3D) and showed highly branched morphology similar to brain microglia[44,45] with no connection to blood vessels (Figures 3C and S3C). We also observed in the posterior lobe more round-shaped macrophages, with only F4/80 expression, which were mainly detected close to blood vessels (Figure S3C).

We investigated the spatial relationship between macrophages and endocrine cells and observed that macrophages were close to luteinizing hormone (LH) producing gonadotrophs, primarily making contact with them through their protrusions surrounding the gonadotrophs (Figure 3D). Furhermore, macrophages were observed to be closely associated with thyrotrophs, producing thyroid-stimulating hormone (TSH). However, unlike the interaction with gonadotrophs, macrophages appeared to exhibit protrusions that connected nearby thyrotrophs, indicating a distinct mode of interaction compared with their association with gonadotrophs (Figures 3E and S3E). Altogether, our findings unveil a particular spatial distribution of phenotypically diverse macrophages within the pituitary gland and suggest potential interactions between macrophages and endocrine cells.

Pituitary gland macrophages originate from early yolk sac progenitors

The ontogeny of pitMØs has not been studied. Therefore, we employed a combination of macrophage reporter mice to unravel the origin and persistence of tissue-resident pitMØs. In the brain, microglia and BAMs derive from yolk sac-origin macrophage progenitors, and in homeostatic conditions, neither of the populations is replaced by monocytes from the bone marrow.[13,35,46] Based on the observed similarities of pitMØs to the brain macrophages, we crossed *Cx3cr1*^{CreERT2} mice[47] to *R26*^{EYFP} or *R26*^{tdTomato} mice[48] to tag the yolk sac erythro-myeloid precursor (EMP) origin macrophages. Pregnant dams were injected with tamoxifen (TAM) to induce irreversible reporter expression in the yolk sac early (TAM E7.5) or late EMPs and their progeny (TAM E8.5 or E9.5). Consistent with a previous report,[46] analyses of the brains of E17.5 embryos, pulse-labeled at E7.5, E8.5, or E9.5, showed high labeling of microglia in the brain (Figures S4A-S4C).

Whole-mount analyses of the pituitary gland at E17.5 showed tdTomato-positive macrophages from E7.5 and at E8.5 pulse labeling, indicating yolk sac-derived macrophages contribute to pitMØs (Figures 4A and 4B). Notably, both pulse labeling time points led to the distribution of tdTomato-positive macrophages throughout the anterior and posterior regions of the pituitary gland (Figures 4A and 4B). Furthermore, labeling initiated at E9.5 revealed EYFP-positive cells exclusively within the pitMØs, with both Ly6C^{Low}MO and Ly6C^{Hi}MO avoiding the labeling (Figures 4C and S4D). EYFP labeling was observed both in CD206^{Pos} (pBAM-MACs) and CD206^{Neg} (including ml-MACs and MHC II^{Neg}-MAC) cells (Figure S4E).

The yolk sac-origin late EMPs not only give rise to non-monocytic yolk sac macrophages[49] but also migrate to the fetal liver to generate fetal liver monocytes.[50] To evaluate embryonic liver monocyte involvement in the pitMØs, we used *Ccr2*^{CreERT2}*; R26*^{tdTomato} reporter mice, which allows the tracking of the Ly6C^{Hi} CCR2^{+} fetal liver-derived monocytes.[13,51] Pregnant *Ccr2*^{CreERT2}*; R26*^{tdTomato} mice were treated with TAM at E14.5 and E16.5. As expected, fetal monocytes in blood, liver, and lung monocyte-origin premature alveolar macrophages (pre-AMs) were tdTomato positive (Figures 4D, S4F–J). A small fraction of Ly6C^{Hi}MO cells was labeled in the pituitary gland (Figure 4D). In contrast, pitMØs showed no labeling, confirming that circulating CCR2-positive fetal liver monocytes do not engraft in the pituitary gland (Figure 4D). To further examine the putative yolk sac origin of the pitMØs, we injected a single dose of function-blocking αCSF1R (AFS98) antibody into

Figure 3. The pituitary gland macrophages are located in unique spatial niches and have close interaction with hormone-secreting cells

(A) Whole-mount immunofluorescence with F4/80, CD206, and MECA-32 from WT pituitary glands at E17.5. Inserts are higher magnifications from the boxed anterior lobe (AL) area. Arrows indicate F4/80^{Pos}CD206^{Neg} cells and arrowheads F4/80^{Pos}CD206^{Pos}. Overview image scale is 100 μm and inserts, 10 μm. Representative images from three independent experiments.

(B) Whole-mount immunofluorescence with P2RY12, CD206, and MECA-32 from WT pituitary glands at NB and 5 weeks of age. Inserts are higher magnifications from the boxed posterior lobe (PL) area. Overview image scales are 100 μm and inserts, 10 μm. Representative images from three independent experiments.

(C) Whole-mount immunofluorescence with P2RY12, MHC II, and MECA-32 from WT pituitary gland of 5 weeks of age. Inserts are higher magnifications from the boxed PL area (I) and the boxed AL area (II). Overview image scale is 100 μm and insert,10 μm. Representative images from three independent experiments.

(D) Whole-mount immunofluorescence with F4/80, LH, and MECA-32 from WT pituitary gland of 5 weeks of age. Inserts are higher magnifications from the boxed AL areas. For overview image, the scale is 100 μm and for inserts, 10 μm. Representative images from three independent experiments.

(E) Whole-mount immunofluorescence with F4/80, TSH, and MECA-32 from WT pituitary gland of 8 weeks of age. Inserts are higher magnifications from the boxed AL area. For overview image, the scale is 100 μm and for inserts, 10 μm. Representative images from three independent experiments.

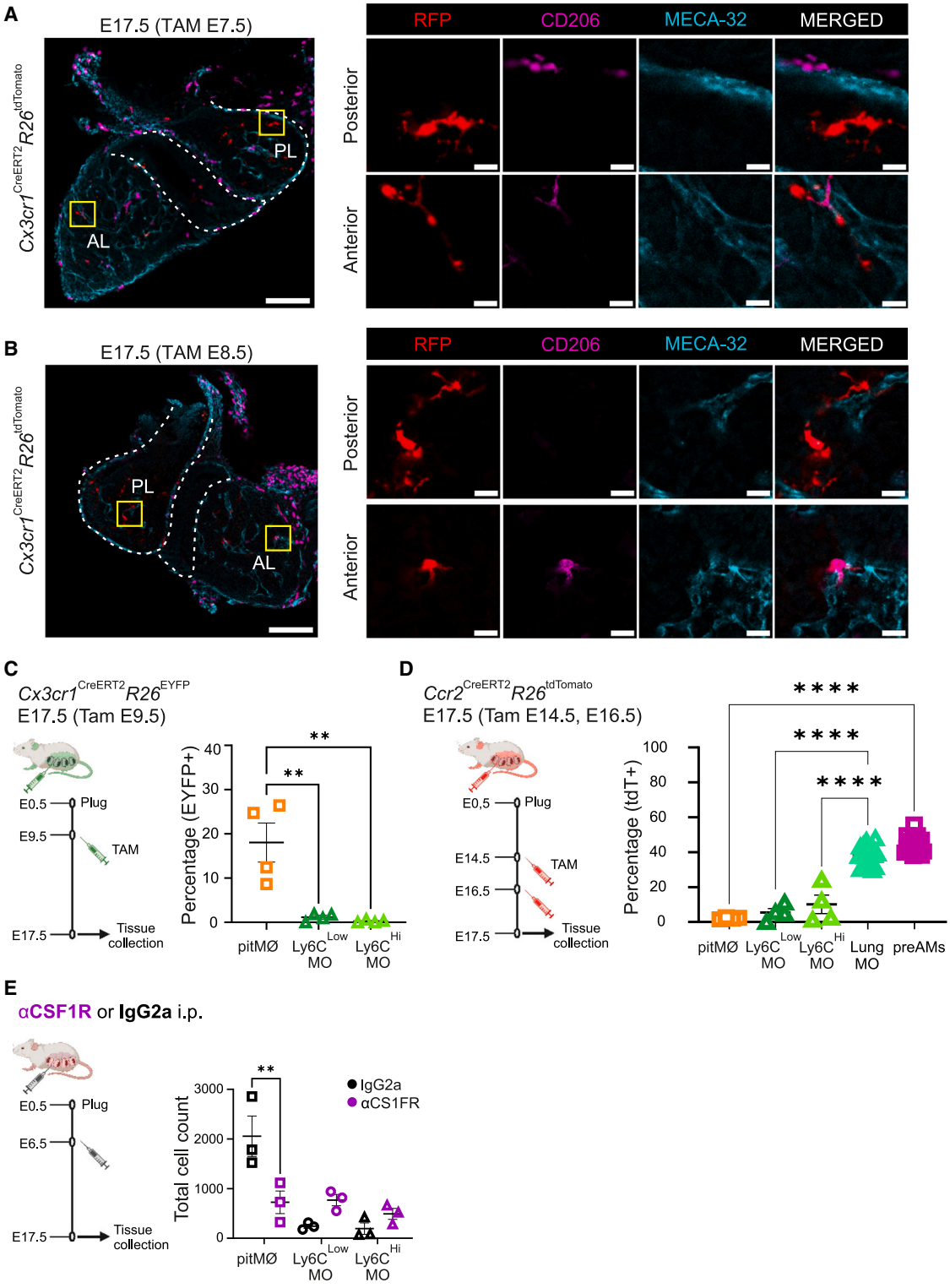

Figure 4. Pituitary gland macrophages originate from early yolk sac progenitors

(A and B) Whole-mount immunofluorescence with RFP, CD206, and MECA-32 from E7.5 (A) or E8.5 (B) TAM-labeled Cx3cr1^{CreERT2}R26^{tdTomato} pituitary glands at E17.5. Inserts are higher magnifications from the boxed PL and AL areas. Overview image scales 100 μm and inserts, 10 μm. Representative images from three independent experiments.

(legend continued on next page)

pregnant WT dams at E6.5 to selectively ablate yolk sac-origin macrophages from the developing embryos. The analyses of E17.5 pituitary glands verified the significant depletion of pitMØs while monocytes remained at the usual level (Figure 4E). Altogether, data show that pitMØs originate from yolk sac EMP descendants, similar to brain microglia and BAMs.

The pituitary gland macrophages are maintained with self-renewing without an input of bone marrow-derived monocytes

Tissue-resident macrophages are maintained in tissues by local self-proliferation or monocyte recruitment from blood circulation.[15,52,53] Whole-mount immunostainings with anti-Ki67 and anti-F4/80 antibodies revealed that proliferating cells were scattered in both the anterior and posterior areas of the pituitary gland (Figures 5A and S5A), showing that pitMØs can undergo *in situ* proliferation. However, in many adult tissues, embryonic-derived tissue-resident macrophages are entirely or partially replenished by bone marrow monocytes recruited from the blood circulation.[53–55] Therefore, we next sought to determine the replenishment of embryonic origin cells and the contribution of adult bone marrow-derived monocytes in the pituitary gland by using *Ms4a3*^{CreERT2}; *R26*^{tdTomato} fate-mapping mice,[56] which allows distinguishing between embryonically seeded (tdTomato^{Neg}) and adult monocyte-derived (tdTomato^{Pos}) macrophages. At 4 weeks of age, *Ms4a3*^{CreERT2}; *R26*^{tdTomato} mice were given intraperitoneal (i.p.) TAM injection for 5 consecutive days. We analyzed the pituitary gland and blood after 4 days from the last injection (Figure 5B). As anticipated, blood monocytes were efficiently tagged (Figures S5B and S5C). However, within the pituitary gland, tdTomato positivity was exclusively observed in the monocyte populations while the pitMØs exhibited no tdTomato positivity (Figure 5C).

As an alternative approach to investigate the replenishment or self-maintenance of embryonic-derived pitMØs through local proliferation in adult mice, we used the *Cx3cr1*^{CreERT2}; *R26*^{EYFP} model. At the age of 4 weeks, *Cx3cr1*^{CreERT2}; *R26*^{EYFP} animals underwent a regimen of TAM administration for 5 consecutive days to ensure a robust and irreversible induction of EYFP in all CX3CR1-positive cells (Figure 5D). Over time, cells developing from blood monocytes after TAM withdrawal are no longer labeled, while long-lived or self-renewing cells will remain EYFP-positive. Five days after the last TAM dose, blood monocytes were EYFP^{+} before being replaced by EYFP^{-} monocytes during the 7 weeks of recovery time (Figure 5E).[47,57] CX3CR1^{+} microglia, which do not undergo replenishment by blood monocytes, retained a high level of EYFP expression even after a 7-week recovery period (Figures S5D and S5E). In the pituitary gland, 5 days post-TAM injections, 65.8% ± 3% of pitMØs were EYFP positive (Figure 5E). Remarkably, even after 7 weeks of recovery, the labeling of pitMØs consistently maintained EYFP positivity, indicating that these macrophages were locally maintained through proliferation (Figure 5E). Further supporting this notion, a single TAM pulse administered at E16.5 resulted in the persistence of EYFP-tagged macrophages at 7 and 14 weeks of age (Figure S5F) and macrophage counts in CCR2-deficient mice, which have severely reduced blood monocyte levels,[58] were unchanged in the pituitary gland (Figure S5G).

To study whether bone marrow-derived monocytes infiltrate the pituitary gland in pathophysiological conditions, we stimulated acute inflammation by i.p. lipopolysaccharide (LPS) injection to adult WT mice. Interestingly, the infection caused an accumulation in pitMØs but did not increase monocyte numbers within the pituitary gland (Figure 5F), despite a significant increment in serum interleukin (IL)-6 levels 24 h after LPS injection (Figure S5H). To exclude the possibility that the elevated macrophage numbers after LPS treatment were due to rapid monocyte turnover into macrophages, we repeated the experiment with *Ms4a3*^{creERT2}; *R26*^{tdTomato} mice (Figures S5I and S5J). While we observed an increased number of pitMØs after LPS injection (Figure S5I), tdTomato-positive cells were exclusively present in the monocyte populations, and no labeling was detected in the pitMØs (Figure S5J). Altogether, these results support the local proliferation of pitMØs and indicate that, even during systemic inflammation, bone marrow-derived monocytes do not contribute to the increase of pitMØs.

Pituitary gland adenomas present the most common disease affecting the pituitary gland.[59] To investigate their impact on pitMØs, we used heterozygous retinoblastoma-deficient (*Rb*$^{+/-}$) mice, known to develop pituitary adenomas with 100% penetrance in older age.[60,61] The *Rb*$^{+/-}$ mice were crossed with *Cx3cr1*^{CreERT2}; *R26*^{EYFP} mice. At 7 months, *Rb*$^{+/-}$; *Cx3cr1*^{CreERT2}; *R26*^{EYFP} mice were treated with TAM for 5 days and analyzed after 8-week recovery (at 9 months; Figure 5G). Interestingly, despite adenoma, total pitMØ and monocyte numbers did not increase (Figures S5K and S5L). Notably, pitMØs remained EYFP-positive long after TAM treatment (Figure 5H). In summary, these findings indicate that pitMØs are self-maintained without input from bone marrow-derived circulating monocytes in adult animals, even in pituitary gland disorders.

Early macrophages function in maintaining hormonal equilibrium within the pituitary gland

We next addressed the functional importance of pitMØs and ablated them with function-blocking αCSF1R antibody. The first

(C) Experimental outline and frequencies of EYFP expression in pitMØ, Ly6C^{Low}MO, and Ly6C^{Hi}MO populations of E9.5 TAM-labeled Cx3cr1^{CreERT2}R26^{EYFP} pituitary glands at E17.5. The quantitative data are mean ± SEM. Each dot represents data from mice pooled together: E17.5 (n = 9–11 mice/pool). Data from four independent experiments.

(D) Experimental outline and frequencies of tdTomato expression in pitMØ, Ly6C^{Low}MO, Ly6C^{Hi}MO, lung monocytes (Lung MO), and pre-alveolar macrophages (preAMs) of E14.5 and E16.5 TAM-labeled Ccr2^{CreERT2}R26^{tdTomato} mice at E17.5. The quantitative data are mean ± SEM. Each dot represents data from mice pooled together (pitMØ, Ly6C^{Low}MO, Ly6C^{Hi}MO, n = 8–10 mice/pool) or individual mice (Lung MO, preAMs, n = 19). Data from four independent experiments.

(E) Experimental outline for treating pregnant dams with blocking CSF1R antibody or control IgG at E6.5. The cell amount of E17.5 pitMØ, Ly6C^{Low}MO, and Ly6C^{Hi}MO cells in the WT mouse pituitary gland after blocking CSF1R antibody or control IgG treatment. The quantitative data are mean ± SEM. Each dot represents data from mice pooled together (n = 8–11 mice/pool). Data from three independent experiments.

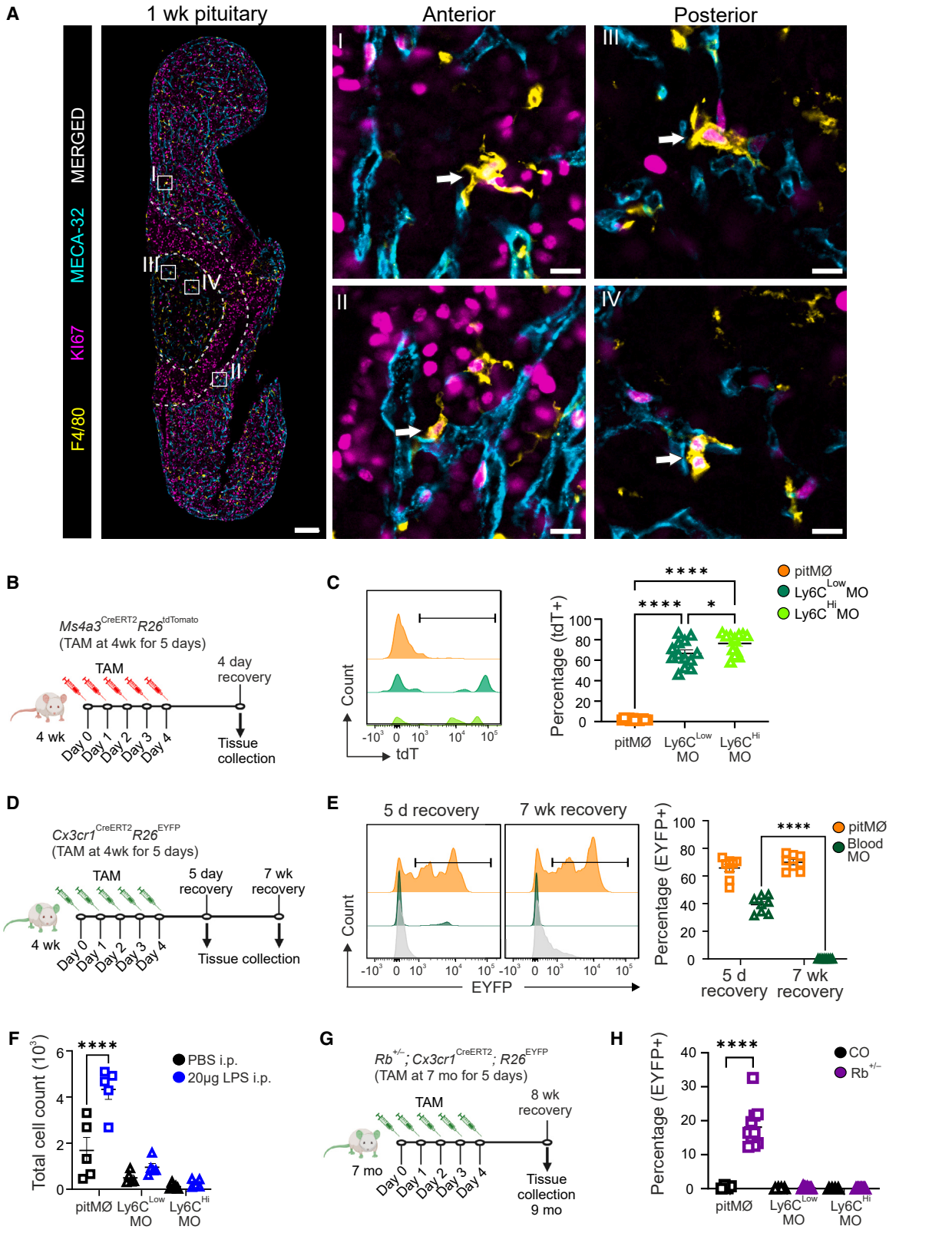

(legend on next page)

injection was given at E6.5 to block the early seeding of macrophages in the pituitary gland. After birth, an αCSF1R antibody was given every second week (four times in total), and tissues were collected 1 week after the last injection (at the age of 5 weeks; Figure 6A). The depletion of macrophages did not yield a noteworthy difference in weight gain between the control and αCSF1R-treated mice (control 17.81 ± 0.45 g vs. 16.47 ± 0.77 g; n = 11–16) or major histological changes in the pituitary gland (Figure S6A). However, the treatment effectively reduced the number of pitMØs (Figure S6B) while the numbers of brain microglia in αCSF1R-treated mice were comparable to those in the control group (Figure S6C). Immunohistochemical analysis did not reveal apparent disparities in the proportions of endocrine cell populations in the macrophage-depleted pituitaries (Figures 6B and S6D–S6F). However, we noted a reduced intensity of LH and TSH staining in macrophage-depleted pituitaries compared with controls (Figures 6B and S6E), while the intensity of prolactin (PRL) staining remained unchanged (Figure S6F). Additionally, the spatial organization of LH-producing gonadotrophs appeared disorganized in macrophage-depleted pituitaries (Figure 6B).

We observed comparable intrapituitary levels of adrenocorticotropic hormone (ACTH), growth hormone (GH), and follicle-stimulating hormone (FSH) between the treated and control mice (Figure 6C). TSH and PRL levels were reduced in the treated group, although the changes were not statistically significant (Figure 6C). In contrast, intrapituitary LH levels showed a slight but significant reduction in the treated group (Figure 6C). Noteworthy is that the depletion of pitMØs reduced significantly only LH but not FSH levels within the pituitary gland, although both are secreted by gonadotrophs.[3] We then restricted macrophage depletion to the embryonic developmental stage. Remarkably, administering the anti-CSF1R antibody once at E6.5 also resulted in a similar trend of reduced intrapituitary hormone levels at 4 weeks of age (Figure S7A). LH is secreted from the pituitary gland into the bloodstream, targeting tissues like the testes. We measured serum hormone levels to assess the impact of reduced intrapituitary LH due to macrophage depletion. However, the decrease in intrapituitary LH was insufficient to significantly lower serum LH, which exhibited only a mild, non-significant trend toward reduction (Figure S7B) and no morphological changes were observed in the testis histology (Figure S7C).

Hypothalamus-released gonadotropin-releasing hormone (GnRH) regulates LH and FSH production in the pituitary gland by stimulating the upregulation and binding the GnRH receptor (GnRHR) on gonadotrophs. Although FSH levels were not affected, we analyzed the *Gnrhr* expression in macrophage-depleted pituitaries to rule out the possibility that reduced intrapituitary LH levels were due to impaired GnRH signaling. Despite the reduction in LH, *Gnrhr* expression remained intact (Figure S7D), indicating that GnRH signaling was unaffected. Collectively, these findings suggest that tissue-resident macrophages play a role in the intricate regulation of hormonal balance within the pituitary gland.

We performed bulk RNA sequencing (bulk RNA-seq) of whole pituitary glands of the anti-CSF1R and control-treated WT mice. Principal-component analysis revealed a difference between anti-CSF1R and control-treated pituitary glands (Figure S7E), having 1,438 differentially expressed genes (DEGs; Table S2). Most of the DEGs (74%; fold change >1.6 adjusted p value <0.1) were downregulated in macrophage-depleted pituitary glands compared with the controls. Among the downregulated genes, a substantial number were core macrophage signature genes, including *Fcgr1*, *Adgre1*, *Mrc1*, *H2-Aa*, and *Csf1r* (Table S2). Within the top DEGs, we identified several genes associated with hormone production in the anterior pituitary that exhibited upregulation in macrophage-depleted pituitary glands (Figures 6D and 6E and Table S2). These include the genes encoding pituitary hormone prolactin (*Prl*), thyrotropin-releasing hormone receptor (*Trhr*), follicle-stimulating hormone beta subunit (*Fshb*), and an orphan G-protein coupled receptor (*Gpr101*), which is involved in the growth of the pituitary gland and stimulus of GH.[62] Moreover, the expression of several transcription factors, including GATA-binding factor 2 (*Gata2*), crucial for gonadotroph and thyrotroph differentiation,[63] early growth response 1 (*Egr-1*), acting as a transcriptional mediator for GnRH-induced signals activating the LHβ gene,[64] and Homeobox Protein (*Oxt1*) implicated in the juvenile stage control of GH, FSH, and LH hormone levels,[65] was enhanced in animals with depleted macrophages (Figure 6E and Table S2).

Elevation of cytosolic calcium (Ca^{2+}) concentration through extracellular Ca^{2+} influx is an essential trigger for hormone secretion and release in pituitary endocrine cells.[66,67] Many genes, such as *Kcnj1* and *Cacng3*, related to extracellular Ca^{2+} influx, were altered in macrophage-depleted pituitary (Figure 6E and

Figure 5. Early yolk sac-derived pituitary gland macrophages self-maintain until late adulthood by proliferation

(A) Whole-mount immunofluorescence with F4/80, proliferation marker KI67, and MECA-32 from WT pituitary glands of 1-week-old mice. Inserts are higher magnifications from the boxed AL area (I-II) and the boxed PL area (III-IV). Arrows indicate F4/80^{Pos}KI67^{Pos} cells. Overview image scales are 100 μm and inserts, 10 μm. Representative images from three independent experiments.

(B and C) Experimental outline, representative histograms, and frequency of tdTomato^{Pos} cells in pitMØ, Ly6C^{Low}MO, and Ly6C^{Hi}MO cells in the Ms4a3^{CreERT2}R26^{tdTomato} mouse pituitary gland at 5 weeks of age (4-day recovery). The quantitative data are mean ± SEM. Each dot represents data from individual mice (n = 13). Data from four independent experiments.

(D and E) Experimental outline, representative histograms, and frequency of EYFP^{Pos} cells in pitMØs and blood monocytes in the Cx3cr1^{CreERT2}R26^{EYFP} mouse pituitary gland at 5 weeks of age (5-day recovery) and 12 weeks of age (7-week recovery). The quantitative data are mean ± SEM. Each dot represents data from individual mice (n = 8). Data from three independent experiments.

(F) Cell amount of pitMØ, Ly6C^{Low}MO, and Ly6C^{Hi}MO cells in the WT mouse pituitary gland at 10 weeks of age after LPS injection (i.p.) and 24-h recovery. The quantitative data are mean ± SEM. Each dot represents data from individual mice (n = 5). Data from three independent experiments.

(G and H) Experimental outline, cell amount, and frequency of EYFP^{Pos} cells in pitMØ, Ly6C^{Low}MO, and Ly6C^{Hi}MO in the Cx3cr1^{CreERT2}R26^{EYFP};Rb$^{-/+}$ mouse pituitary gland at 9 months of age. The quantitative data are mean ± SEM. Each dot represents data from individual mice (n = 4–10). Data from three independent experiments.

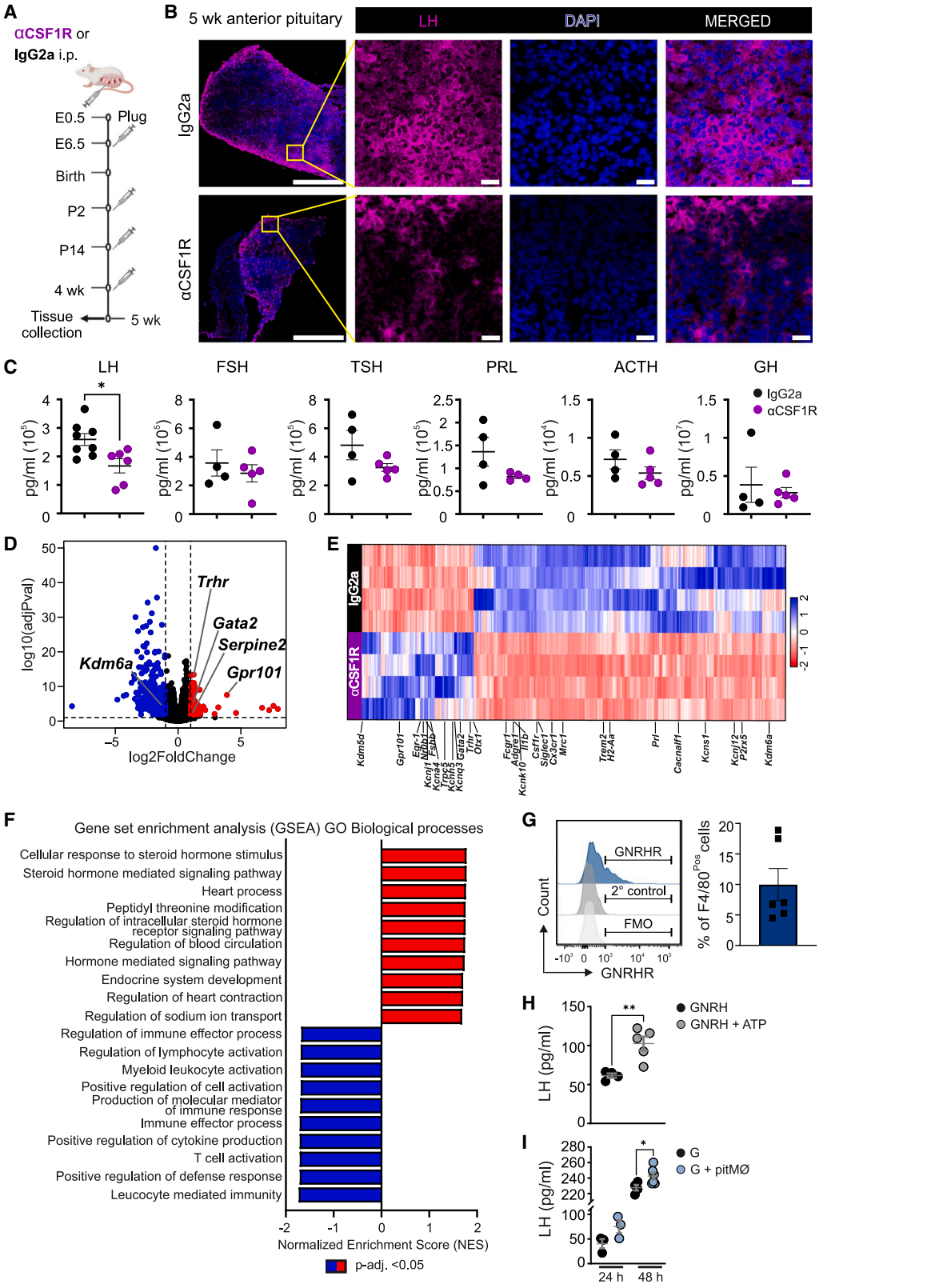

(legend on next page)

Table S2). Interestingly, the expression of *Trpc5* (short transient receptor potential channel 5) and *Kcnq3* (potassium voltage-gated channel subfamily Q member 3), key regulators of membrane depolarization and intracellular Ca^{2+} increase in gonadotrophs under GnRH stimulation, was upregulated in macrophage-depleted pituitary glands. Notably, *P2rx5* (purinergic receptor P2X, ligand-gated ion channel, 5), which is primarily activated by extracellular adenosine triphosphate (ATP) and mainly found in LH and TSH cells in the anterior pituitary,[68] was downregulated (Figure 6E and Table S2).

In gene set enrichment analysis (GSEA), anti-CSF1R-treated pituitary glands showed significant downregulation of immunological functions such as T cell activation and positive regulation of cytokine production (Figure 6F). Conversely, the upregulated biological pathways were linked to hormonal regulation, encompassing cellular responses to steroids, steroid hormone-mediated signaling pathways, regulation of intracellular steroid hormone receptor signaling pathways, and endocrine system development (Figure 6F). Among the top-regulated biological pathways were also many related to ion transport (Figure 6F). To ensure the consistency of the bioinformatic analysis, we performed reactome annotations and ingenuity pathway analysis (IPA) on the DEGs (Figure S7F and Table S3), which showed similar results to those obtained from GSEA.

Notably, we identified a subset of pitMØs expressing GNRHR, indicating their potential capability to respond to GnRH stimulation (Figure 6G). We isolated the total pitMØs and gonadotrophs (live/$CD45^{-}$/$GNRHR^{+}$) from the adult WT male mice and cultured *in vitro* the gonadotrophs and pitMØs either independently or in co-culture. Following an overnight incubation, we measured extracellular ATP from the culture medium. Our findings revealed that pitMØs secrete low levels of extracellular ATP under basal conditions, increasing upon stimulation with 10 μM GnRH (Figure S7G). Co-culturing gonadotrophs with pitMØs resulted in higher basal ATP levels than gonadotrophs alone (Figure S7H). Furthermore, when gonadotrophs were stimulated with GnRH and ATP, LH levels were significantly enhanced (Figure 6H). We then cultured gonadotrophs or gonadotrophs and pitMØs in co-cultures. After 1- or 2-day incubation, cells were treated with 10 μM GnRH for 3 h before collecting medium for LH measurements. Notably, after 24 h of co-culture, LH release was higher in the presence of pitMØs, with a more pronounced increase after 48 h (Figure 6I). Collectively, our data indicate that the depletion of macrophages in the pituitary gland disrupts the balance of hormone production, highlighting a previously unrecognized role of tissue-resident macrophages in maintaining pituitary gland homeostasis.

DISCUSSION

Although macrophages have been reported in the pituitary gland,[26,30,31,39,69] most of these studies have lacked sufficient resolution to profile the pituitary gland macrophage compartment comprehensively. In this study, we employed a combination of approaches to highlight the presence of transcriptionally and spatially variable resident macrophage subsets within the pituitary gland, showing dynamic phenotypic changes from neonatal to adulthood. Our results unveiled a distinct contrast in the transcriptional profiles of macrophage subpopulations between the anterior and posterior lobes and highlighted a notable divergence in their molecular characteristics. In the posterior pituitary lobe, which serves as a neuroendocrine interface, we identified a homogeneous ml-MAC macrophage subset that exhibited transcriptional and morphological similarities to microglia in the central nervous system (CNS).[32–35] This similarity is likely attributed to the embryological and anatomical continuity between the posterior pituitary and hypothalamus. In contrast, the anterior pituitary gland, which functions as a hormone-producing organ, exhibited greater transcriptional, kinetic, and spatial heterogeneity among pitMØs than previously recognized.[30,69,70] Fate-mapping analyses revealed that pitMØs originate solely from early yolk sac precursors and persists throughout the lifespan by local proliferation, even in pathophysiological conditions. Moreover, our findings demonstrated that depleting pitMØs has profound consequences on the hormonal balance of the pituitary gland.

The initial wave of embryonic macrophages originates from early yolk sac myeloid precursors around E7.0. Following the establishment of the bloodstream around E9.5, primitive macrophages migrate into the developing tissues, and in the brain, they

Figure 6. The presence of early macrophages plays a crucial role in maintaining hormonal equilibrium within the postnatal pituitary gland

(A) Experimental outline for treating WT mice with blocking CSF1R antibody or control IgG at E6.5, P2, P14, and 4 weeks of age.

(B) Frozen section immunofluorescence staining with anti-LHβ and nuclear marker DAPI from the pituitary gland of 5-week-old WT mice after treatment with blocking CSF1R antibody or control IgG at E6.5, P2, P14, and 4 weeks of age. Inserts are higher magnifications from the boxed AL areas. Overview image scale 500 μm and inserts, 20 μm. Representative images from three independent experiments.

(C) Intrapituitary hormone measurements for LH, FSH, TSH, PRL, ACTH, and GH from the pituitary gland of 5-week-old WT mice after treatment with blocking CSF1R antibody or control IgG at E6.5, P2, P14, and 4 weeks of age. The quantitative data are mean ± SEM. Each dot represents data from individual mice (n = 4–8). Data from four (LH) and three (others) independent experiments.

(D and E) Volcano plot (E) and heatmap (F) of the DEGs between the pituitary glands of 5-week-old WT mice after treatment with blocking CSF1R antibody or control IgG at E6.5, P2, P14, and 4 weeks of age. Data from individual mice (n = 4).

(F) GSEA analyses (GO Biological processes) of the bulk RNA-seq data. Gene sets ranked according to their normalized enrichment scores (NES).

(G) Representative histogram for GNRHR (blue) shown with secondary Donkey Anti-Rabbit IgG AF647 control (dark gray), Fluorescence Minus One (FMO) control (light gray), and frequency of GNRHR positive cells in pitMØs in the pituitary gland of adult WT mice. The quantitative data are mean ± SEM. Each dot represents data from individual mice (n = 6). Data from three independent experiments.

(H) LH measurements from *in vitro* experiments of gonadotroph ($GNRHR^{pos}$) cells after 3 h stimulated with GnRH or GnRH together with ATP. The quantitative data are mean ± SEM. Each dot represents data from mice pooled together (n = 8–18 mice/pool). Data from three independent experiments.

(I) LH measurements from *in vitro* experiments of gonadotrophs or gonadotrophs and pitMØs in co-cultures after stimulation with GnRH on 24-h or 48-h incubation time. The quantitative data are mean ± SEM. Each dot represents data from mice pooled together (n = 8–12 mice/pool). Data from three independent experiments.

undergo differentiation to form microglia.[46,50] In other tissues, early yolk sac macrophages are predominantly substituted in the later stages of development by monocyte-derived macrophages originating from the fetal liver.[71] Post-birth, over time, embryonic-derived macrophages are either entirely or partially displaced by CCR2-dependent Ly6C^{Hi} monocyte-derived macrophages.[53,72] However, microglial cells stand out as distinctive exceptions among tissue-resident macrophages. In a state of homeostasis, these cells retain their yolk sac origin throughout adulthood.[46] Using advanced genetic lineage tracing, we show that, similarly to microglia,[13,36,46,73,74] both posterior or anterior pitMØs originate from primitive yolk sac-derived macrophages and are not displaced by fetal liver monocyte-derived macrophages, although the pituitary gland is outside the blood-brain-barrier. Moreover, we found that renewal of the adult pituitary gland macrophage compartment during steady state does not necessitate any contribution from bone marrow monocytes.

In a few tissues, such as the skin,[75] lung alveolar space,[47,76] and brain,[46] only minor or no monocytes are observed under physiological conditions. However, in various disease states, including those affecting the brain, bone marrow-derived monocytes can infiltrate these tissues and differentiate into macrophages.[77] In the brain, BAMs have proven to be renewed through monocyte recruitment in adulthood and aging.[36,77] Interestingly, despite the small and steady amount of monocytes in the pituitary and sustained macrophage depletion, monocyte-derived cells did not contribute to replenishing the empty macrophage niche in the pituitary gland. While microglial cells demonstrated re-population during the 2-week recovery period following each antibody injection, pitMØs did not undergo replenishment within the same time frame. It has been shown that the number of macrophages increases in the pituitary gland 6–24 h after LPS injection and returns to normal levels 48 h after.[78] We observed the accumulation of pitMØs at 24 h when mice were subjected to acute LPS-induced inflammation, but even then, monocyte influx into the pituitary gland was not observed. The outcome was unexpected, as it has been shown that systemic exposure to LPS induces the migration of inflammatory monocytes throughout various tissues, including the brain.[79] Tumor-derived factors have been shown to attract circulating CCR2-expressing inflammatory monocytes into the tumor environment, where they differentiate into macrophages.[80,81] Mice heterozygous for the retinoblastoma gene (*Rb*) develop ACTH-producing aggressive tumors arising from the intermediate lobe of the pituitary with high incidence from ages 2 to 11 months.[60,61] Our studies reveal that tumor development in retinoblastoma-deficient mice did not increase the overall numbers of pitMØs or monocytes. Moreover, results from *Rb*$^{+/-}$; *Cx3cr1*^{CreERT2}; *R26*^{EYFP} mice showed that, in agreement with the cell fate data, pitMØs showed no contribution from monocytes even with increasing age. Hence, our findings strongly suggest that pitMØs are maintained independently of bone marrow-derived monocytes, and even under pathophysiological conditions, increasing monocyte infiltration is not evident in the pituitary gland. However, it remains a possibility that prolonged LPS treatment or different types of pituitary tumors could result in increased monocyte migration within the pituitary gland.

Our research indicates that prolonged macrophage depletion disrupts the delicate networks of LH-producing gonadotrophs, reducing intrapituitary LH levels. During pituitary gland development, secretory cells form organized three-dimensional network structures that play a functional role in integrating, amplifying, and transmitting signals.[6,82–84] Our findings reveal that macrophages are positioned near gonadotrophs within the spatial microenvironment, suggesting that they shape localized microenvironments that facilitate cellular communication. One component of this paracrine signaling can be extracellular ATP/ADP, which is crucial in mediating crosstalk between neighboring cells in many tissues.[33,73,74] In gonadotrophs, extracellular ATP has been shown to enhance GnRH-induced Ca^{2+} signaling by activating the ligand-gated P2X receptor channels (P2XRs), leading to an increase in cytosolic Ca^{2+} levels.[66,67,85] Notably, a reduction of extracellular Ca^{2+} has been shown to cause a prompt decline in LH production.[86–89] However, the physiological sources of extracellular ATP responsible for activating purinergic receptors in the pituitary gland are not yet fully understood. Our *in vitro* experiments demonstrated that similar to macrophages in other tissues,[90–92] pituitary gland macrophages can release ATP into the extracellular space, and this release was further enhanced upon GnRH stimulation. Therefore, macrophage depletion within the pituitary gland potentially disrupts calcium homeostasis by decreasing the availability of extracellular ATP in the local microenvironment, affecting the signaling dynamics between the cells similar to the "purinergic microglia-neuron junctions" phenomenon recently discovered in the mouse brain.[93,94] *In vitro* co-culture experiments of macrophages and gonadotrophs revealed that LH production increased significantly within just 1 day of co-culture. However, extending the culture period led to substantial rise in LH levels. The kinetical increase in LH production supports the idea that the spatial organization of these cells is critical for their interaction. The outstanding challenge now for the future is to define the intercellular communication between macrophages and different hormone-producing cells in the delicate *in vivo* 3D environment of the pituitary gland.

Tissue-specific depletion of macrophages is still limited, and models like *P2ry12*^{CreER}[95] or *Sall1*^{CreER},[33] which can be used to increase specificity for microglia depletion in the brain, are not currently available for the anterior pituitary. Therefore, we employed antibody-based approach to deplete macrophages within the pituitary gland. Given the known limitation of αCSF1R in causing systemic macrophage depletion,[96] our strategy was specifically designed to preserve brain-resident macrophages, thereby avoiding interference with hypothalamic regulation of the pituitary gland and broader neuroendocrine functions. However, the limitation of this approach was its inability to achieve complete macrophage depletion within the pituitary, as approximately 17% of macrophages remained in tissue, which may account for only partial effects on intrapituitary and serum hormonal levels observed in our model. In the future, it will be valuable to investigate the outcomes of complete macrophage depletion in the pituitary gland to understand its full impact on the system.

In summary, we provide a transcriptomic characterization of pitMØs, highlighting their diverse features. The pituitary gland

contains spatially distinct macrophages: ml-MACs with microglia-like genes in the posterior lobe and other pitMØs in the anterior lobe closely interacting with hormone-secreting cells. All pitMØs originate from yolk sac progenitors and self-renew independently of bone marrow-derived monocytes. These findings underscore the significance of pitMØs in regulating hormone production and intercellular communication. However, further research into the specific mechanisms by which macrophages exert these effects will provide valuable insights into pituitary physiology and may uncover potential therapeutic targets for hormone-related disorders.

Limitations of the study

In bulk RNA seq, the anterior and posterior pituitary regions were not distinguished and observed gene expression changes likely reflect both regions. Validation should be done using spatial transcriptomics or protein-level analyses. Advanced models are needed to explore macrophage interactions with hormonal cells in the pituitary and to study long-term hormonal effects after macrophage depletion. Current models do not allow for studying the 3D networks of hormone-secreting cells or selective manipulation of specific pituitary cell types.

RESOURCE AVAILABILITY

Lead contact

Further information and requests for resources and reagents should be directed to the lead contact, Pia Rantakari (pia.rantakari@utu.fi).

Materials availability

This study did not generate new unique reagents.

Data and code availability

Single-cell RNA-seq and bulk RNA-seq data have been deposited at the NCBI Gene Expression Omnibus. The accession numbers are listed in the key resources table. This paper does not report the original code.

ACKNOWLEDGMENTS

We thank Laura Grönfors and Etta-Liisa Väänänen for technical help and acknowledge the Cell Imaging and Cytometry Core, The Single Cell Omics Core, and The Functional Genomics Core (Turku Bioscience, University of Turku, Åbo Akademi University, and Biocenter Finland) for services, instrumentation, and expertise. We thank Prof. Jorma Toppari for kindly providing us with the $Rb^{+/-}$ mouse model. The Research Council of Finland, the Sigrid Jusélius Foundation, The Jane and Aatos Erkko Foundation, and the Turku Doctoral Program of Molecular Medicine financially supported this study.

AUTHOR CONTRIBUTIONS

H.L. conducted experiments, analyzed data, and helped prepare the manuscript. H.J. designed and conducted experiments, analyzed data, supervised the study, and wrote the manuscript. J.H. and A.M. performed scRNA-seq and bulk RNA-seq analyses, respectively. L.T. assisted with experiments and manuscript preparation. M.S. acquired funding, supervised the study, and edited the manuscript. F.G., B.B., and M.G. provided mouse models and edited the manuscript. G.G.Y. performed ATP experiments and analyses. H.G. assisted with experiments. P.R. conceived, funded, and supervised the study, and wrote the manuscript. All authors approved the final manuscript.

DECLARATION OF INTERESTS

The authors declare no competing interests.

STAR★METHODS

Detailed methods are provided in the online version of this paper and include the following:

- KEY RESOURCES TABLE
- EXPERIMENTAL MODEL AND STUDY PARTICIPANT DETAILS
  - Mice
  - Primary cell culture
- METHOD DETAILS
  - Single-cell isolation
  - ScRNA sequencing and data analysis
  - In utero and adult tamoxifen administration
  - Flow cytometry
  - Immunofluorescence staining and confocal microscopy
  - X-gal staining
  - LPS treatment
  - Antibody treatment experiments
  - Histological analyses
  - Bulk RNA sequencing and data analysis
  - Hormone measurements
  - mRNA expression by quantitative real-time PCR
  - *In vitro* ATP measurements
  - *In vitro* LH determination
- QUANTIFICATION AND STATISTICAL ANALYSIS
  - Statistical analyses

SUPPLEMENTAL INFORMATION

Supplemental information can be found online at https://doi.org/10.1016/j.celrep.2024.115227.

Received: May 14, 2024
Revised: November 26, 2024
Accepted: December 30, 2024

REFERENCES

1. Kelberman, D., Rizzoti, K., Lovell-Badge, R., Robinson, I.C.A.F., and Dattani, M.T. (2009). Genetic regulation of pituitary gland development in human and mouse. Endocr. Rev. *30*, 790–829. https://doi.org/10.1210/er.2009-0008.
2. Davis, S.W., Ellsworth, B.S., Peréz Millan, M.I., Gergics, P., Schade, V., Foyouzi, N., Brinkmeier, M.L., Mortensen, A.H., and Camper, S.A. (2013). Pituitary gland development and disease: from stem cell to hormone production. Curr. Top. Dev. Biol. *106*, 1–47. https://doi.org/10.1016/B978-0-12-416021-7.00001-8.
3. Le Tissier, P., Campos, P., Lafont, C., Romanò, N., Hodson, D.J., and Mollard, P. (2017). An updated view of hypothalamic–vascular–pituitary unit function and plasticity. Nat. Rev. Endocrinol. *13*, 257–267. https://doi.org/10.1038/nrendo.2016.193.
4. Rizzoti, K., and Lovell-Badge, R. (2005). Early development of the pituitary gland: Induction and shaping of Rathke's pouch. Rev. Endocr. Metab. Disord. *6*, 161–172. https://doi.org/10.1007/s11154-005-3047-7.
5. Perez-Castro, C., Renner, U., Haedo, M.R., Stalla, G.K., and Arzt, E. (2012). Cellular and Molecular Specificity of Pituitary Gland Physiology. Physiol. Rev. *92*, 1–38. https://doi.org/10.1152/physrev.00003.2011.
6. Le Tissier, P.R., Hodson, D.J., Lafont, C., Fontanaud, P., Schaeffer, M., and Mollard, P. (2012). Anterior pituitary cell networks. Front. Neuroendocrinol. *33*, 252–266. https://doi.org/10.1016/j.yfrne.2012.08.002.
7. Mass, E., Nimmerjahn, F., Kierdorf, K., and Schlitzer, A. (2023). Tissue-specific macrophages: how they develop and choreograph tissue biology. Nat. Rev. Immunol. *23*, 563–579. https://doi.org/10.1038/s41577-023-00848-y.

8. Lazarov, T., Juarez-Carreño, S., Cox, N., and Geissmann, F. (2023). Physiology and diseases of tissue-resident macrophages. Nature *618*, 698–707. https://doi.org/10.1038/s41586-023-06002-x.

9. Park, M.D., Silvin, A., Ginhoux, F., and Merad, M. (2022). Macrophages in health and disease. Cell *185*, 4259–4279. https://doi.org/10.1016/j.cell.2022.10.007.

10. Hoe, G., Ginhoux, F., Hoeffel, G., Ginhoux, F., Hoe, G., Ginhoux, F., Hoeffel, G., and Ginhoux, F. (2018). Fetal monocytes and the origins of tissue-resident macrophages. Cell. Immunol. *330*, 5–15. https://doi.org/10.1016/j.cellimm.2018.01.001.

11. Jenkins, S.J., and Allen, J.E. (2021). The expanding world of tissue-resident macrophages. Eur. J. Immunol. *51*, 1882–1896. https://doi.org/10.1002/eji.202048881.

12. Guilliams, M., Thierry, G.R., Bonnardel, J., and Bajenoff, M. (2020). Establishment and Maintenance of the Macrophage Niche. Immunity *52*, 434–451. https://doi.org/10.1016/j.immuni.2020.02.015.

13. Utz, S.G., See, P., Mildenberger, W., Thion, M.S., Silvin, A., Lutz, M., Ingelfinger, F., Rayan, N.A., Lelios, I., Buttgereit, A., et al. (2020). Early Fate Defines Microglia and Non-parenchymal Brain Macrophage Development. Cell *181*, 557–573.e18. https://doi.org/10.1016/j.cell.2020.03.021.

14. Ensan, S., Li, A., Besla, R., Degousee, N., Cosme, J., Roufaiel, M., Shikatani, E.A., El-Maklizi, M., Williams, J.W., Robins, L., et al. (2016). Self-renewing resident arterial macrophages arise from embryonic CX3CR1(+) precursors and circulating monocytes immediately after birth. Nat. Immunol. *17*, 159–168. https://doi.org/10.1038/ni.3343.

15. Dick, S.A., Macklin, J.A., Nejat, S., Momen, A., Clemente-Casares, X., Althagafi, M.G., Chen, J., Kantores, C., Hosseinzadeh, S., Aronoff, L., et al. (2019). Self-renewing resident cardiac macrophages limit adverse remodeling following myocardial infarction. Nat. Immunol. *20*, 29–39. https://doi.org/10.1038/s41590-018-0272-2.

16. Evren, E., Ringqvist, E., Doisne, J.-M., Thaller, A., Sleiers, N., Flavell, R.A., Di Santo, J.P., and Willinger, T. (2022). CD116+ fetal precursors migrate to the perinatal lung and give rise to human alveolar macrophages. J. Exp. Med. *219*, e20210987. https://doi.org/10.1084/jem.20210987.

17. Jäppinen, N., Félix, I., Lokka, E., Tyystjärvi, S., Pynttäri, A., Lahtela, T., Gerke, H., Elima, K., Rantakari, P., and Salmi, M. (2019). Fetal-derived macrophages dominate in adult mammary glands. Nat. Commun. *10*, 281. https://doi.org/10.1038/s41467-018-08065-1.

18. Félix, I., Jokela, H., Karhula, J., Kotaja, N., Savontaus, E., Salmi, M., and Rantakari, P. (2021). Single-Cell Proteomics Reveals the Defined Heterogeneity of Resident Macrophages in White Adipose Tissue. Front. Immunol. *12*, 1–17. https://doi.org/10.3389/fimmu.2021.719979.

19. Zhu, Y., Herndon, J.M., Sojka, D.K., Kim, K.W., Knolhoff, B.L., Zuo, C., Zhu, Y., Herndon, J.M., Sojka, D.K., Lavine, K.J., and Cullinan, D.R. (2017). Tissue-resident macrophages in pancreatic ductal adenocarcinoma originate from embryonic hematopoiesis and promote tumor progression. Immunity *47*, 323–338.e6. https://doi.org/10.1016/j.immuni.2017.07.014.

20. Jokela, H., Lokka, E., Kiviranta, M., Tyystjärvi, S., Gerke, H., Elima, K., Salmi, M., and Rantakari, P. (2020). Fetal-derived macrophages persist and sequentially maturate in ovaries after birth in mice. Eur. J. Immunol. *50*, 1500–1514. https://doi.org/10.1002/eji.202048531.

21. Lokka, E., Lintukorpi, L., Cisneros-Montalvo, S., Mäkelä, J.A., Tyystjärvi, S., Ojasalo, V., Gerke, H., Toppari, J., Rantakari, P., and Salmi, M. (2020). Generation, localization and functions of macrophages during the development of testis. Nat. Commun. *11*, 4375. https://doi.org/10.1038/s41467-020-18206-0.

22. Dolfi, B., Gallerand, A., Firulyova, M.M., Xu, Y., Merlin, J., Dumont, A., Castiglione, A., Vaillant, N., Quemener, S., Gerke, H., et al. (2022). Unravelling the sex-specific diversity and functions of adrenal gland macrophages. Cell Rep. *39*, 110949. https://doi.org/10.1016/j.celrep.2022.110949.

23. Mossadegh-Keller, N., Gentek, R., Gimenez, G., Bigot, S., Mailfert, S., and Sieweke, M.H. (2017). Developmental origin and maintenance of distinct testicular macrophage populations. J. Exp. Med. *214*, 2829–2841. https://doi.org/10.1084/jem.20170829.

24. Wang, M., Yang, Y., Cansever, D., Wang, Y., Kantores, C., Messiaen, S., Moison, D., Livera, G., Chakarov, S., Weinberger, T., et al. (2021). Two populations of self-maintaining monocyte-independent macrophages exist in adult epididymis and testis. Proc. Natl. Acad. Sci. USA *118*, e2013686117. https://doi.org/10.1073/pnas.2013686117.

25. Rehman, A., Pacher, P., and Haskó, G. (2021). Role of Macrophages in the Endocrine System. Trends in Endocrinology & Metabolism *32*, 238–256. https://doi.org/10.1016/j.tem.2020.12.001.

26. Hume, D.A., Halpintt, D., Charltont, H., and Gordon, S. (1984). The mononuclear phagocyte system of the mouse defined by immunohistochemical localization of antigen F4/80: Macrophages of endocrine organs (pituitary/adrenal cortex/corpus luteum/testis). Proc. Natl. Acad. Sci. USA *81*, 4174–4177.

27. Turner, E.C., Hughes, J., Wilson, H., Clay, M., Mylonas, K.J., Kipari, T., Duncan, W.C., and Fraser, H.M. (2011). Conditional ablation of macrophages disrupts ovarian vasculature. Reproduction *141*, 821–831. https://doi.org/10.1530/REP-10-0327.

28. DeFalco, T., Potter, S.J., Williams, A.V., Waller, B., Kan, M.J., and Capel, B. (2015). Macrophages Contribute to the Spermatogonial Niche in the Adult Testis. Cell Rep. *12*, 1107–1119. https://doi.org/10.1016/j.celrep.2015.07.015.

29. Gu, X., Heinrich, A., Li, S.Y., and DeFalco, T. (2023). Testicular macrophages are recruited during a narrow fetal time window and promote organ-specific developmental functions. Nat. Commun. *14*, 1439. https://doi.org/10.1038/s41467-023-37199-0.

30. Principe, M., Chanal, M., Ilie, M.D., Ziverec, A., Vasiljevic, A., Jouanneau, E., Hennino, A., Raverot, G., and Bertolino, P. (2020). Immune Landscape of Pituitary Tumors Reveals Association Between Macrophages and Gonadotroph Tumor Invasion. J. Clin. Endocrinol. Metab. *105*, dgaa520. https://doi.org/10.1210/clinem/dgaa520.

31. Fujiwara, K., Yatabe, M., Tofrizal, A., Jindatip, D., Yashiro, T., and Nagai, R. (2017). Identification of M2 macrophages in anterior pituitary glands of normal rats and rats with estrogen-induced prolactinoma. Cell Tissue Res. *368*, 371–378. https://doi.org/10.1007/s00441-016-2564-x.

32. Hammond, T.R., Dufort, C., Dissing-Olesen, L., Giera, S., Young, A., Wysoker, A., Walker, A.J., Gergits, F., Segel, M., Nemesh, J., et al. (2019). Single-Cell RNA Sequencing of Microglia throughout the Mouse Lifespan and in the Injured Brain Reveals Complex Cell-State Changes. Immunity *50*, 253–271.e6. https://doi.org/10.1016/j.immuni.2018.11.004.

33. Buttgereit, A., Lelios, I., Yu, X., Vrohlings, M., Krakoski, N.R., Gautier, E.L., Nishinakamura, R., Becher, B., and Greter, M. (2016). Sall1 is a transcriptional regulator defining microglia identity and function. Nat. Immunol. *17*, 1397–1406. https://doi.org/10.1038/ni.3585.

34. Lavin, Y., Winter, D., Blecher-Gonen, R., David, E., Keren-Shaul, H., Merad, M., Jung, S., and Amit, I. (2014). Tissue-resident macrophage enhancer landscapes are shaped by the local microenvironment. Cell *159*, 1312–1326. https://doi.org/10.1016/J.CELL.2014.11.018.

35. Brioschi, S., Belk, J.A., Peng, V., Molgora, M., Rodrigues, P.F., Nguyen, K.M., Wang, S., Du, S., Wang, W.-L., Grajales-Reyes, G.E., et al. (2023). A Cre-deleter specific for embryo-derived brain macrophages reveals distinct features of microglia and border macrophages. Immunity *56*, 1027–1045.e8. https://doi.org/10.1016/j.immuni.2023.01.028.

36. Van Hove, H., Martens, L., Scheyltjens, I., De Vlaminck, K., Pombo Antunes, A.R., De Prijck, S., Vandamme, N., De Schepper, S., Van Isterdael, G., Scott, C.L., et al. (2019). A single-cell atlas of mouse brain macrophages reveals unique transcriptional identities shaped by ontogeny and tissue environment. Nat. Neurosci. *22*, 1021–1035. https://doi.org/10.1038/s41593-019-0393-4.

37. Weiler, P., Lange, M., Klein, M., Pe'er, D., and Theis, F.J. (2024). Unified fate mapping in multiview single-cell data. Nat. Methods *21*, 1196–1205.

38. Wolf, F.A., Hamey, F.K., Plass, M., Solana, J., Dahlin, J.S., Göttgens, B., Rajewsky, N., Simon, L., and Theis, F.J. (2019). PAGA: graph abstraction reconciles clustering with trajectory inference through a topology preserving map of single cells. Genome Biol. *20*, 59. https://doi.org/10.1186/s13059-019-1663-x.

39. Chen, Q., Leshkowitz, D., Blechman, J., and Levkowitz, G. (2020). Single-cell molecular and cellular architecture of the mouse neurohypophysis. eNeuro *7*, 1–14. https://doi.org/10.1523/ENEURO.0345-19.2019.

40. Dai, X.-M., Ryan, G.R., Hapel, A.J., Dominguez, M.G., Russell, R.G., Kapp, S., Sylvestre, V., and Stanley, E.R. (2002). Targeted disruption of the mouse colony-stimulating factor 1 receptor gene results in osteopetrosis, mononuclear phagocyte deficiency, increased primitive progenitor cell frequencies, and reproductive defects. Blood *99*, 111–120. https://doi.org/10.1182/blood.v99.1.111.

41. Wiktor-Jedrzejczak, W., Bartocci, A., Ferrante, A.W., Ahmed-Ansari, A., Sell, K.W., Pollard, J.W., and Stanley, E.R. (1990). Total absence of colony-stimulating factor 1 in the macrophage-deficient osteopetrotic (op/op) mouse. Proc. Natl. Acad. Sci. USA *87*, 4828–4832. https://doi.org/10.1073/pnas.87.12.4828.

42. Wang, Y., Szretter, K.J., Vermi, W., Gilfillan, S., Rossini, C., Cella, M., Barrow, A.D., Diamond, M.S., and Colonna, M. (2012). IL-34 is a tissue-restricted ligand of CSF1R required for the development of Langerhans cells and microglia. Nat. Immunol. *13*, 753–760. https://doi.org/10.1038/ni.2360.

43. Greter, M., Lelios, I., Pelczar, P., Hoeffel, G., Price, J., Leboeuf, M., Kündig, T.M., Frei, K., Ginhoux, F., Merad, M., and Becher, B. (2012). Stroma-derived interleukin-34 controls the development and maintenance of langerhans cells and the maintenance of microglia. Immunity *37*, 1050–1060. https://doi.org/10.1016/j.immuni.2012.11.001.

44. Gu, N., Eyo, U.B., Murugan, M., Peng, J., Matta, S., Dong, H., and Wu, L.-J. (2016). Microglial P2Y12 receptors regulate microglial activation and surveillance during neuropathic pain. Brain Behav. Immun. *55*, 82–92. https://doi.org/10.1016/j.bbi.2015.11.007.

45. Peng, J., Liu, Y., Umpierre, A.D., Xie, M., Tian, D.-S., Richardson, J.R., and Wu, L.-J. (2019). Microglial P2Y12 receptor regulates ventral hippocampal CA1 neuronal excitability and innate fear in mice. Mol. Brain *12*, 71. https://doi.org/10.1186/s13041-019-0492-x.

46. Ginhoux, F., Greter, M., Leboeuf, M., Nandi, S., See, P., Gokhan, S., Mehler, M.F., Conway, S.J., Ng, L.G., Stanley, E.R., et al. (2010). Fate mapping analysis reveals that adult microglia derive from primitive macrophages. Science *330*, 841–845. https://doi.org/10.1126/science.1194637.

47. Yona, S., Kim, K.W., Wolf, Y., Mildner, A., Varol, D., Breker, M., Strauss-Ayali, D., Viukov, S., Guilliams, M., Misharin, A., et al. (2013). Fate mapping reveals origins and dynamics of monocytes and tissue macrophages under homeostasis. Immunity *38*, 79–91. https://doi.org/10.1016/j.immuni.2012.12.001.

48. Srinivas, S., Watanabe, T., Lin, C.-S., William, C.M., Tanabe, Y., Jessell, T.M., and Costantini, F. (2001). Cre reporter strains produced by targeted insertion of EYFP and ECFP into the ROSA26 locus. BMC Dev. Biol. *1*, 4. https://doi.org/10.1186/1471-213X-1-4.

49. Mass, E., Ballesteros, I., Farlik, M., Halbritter, F., Günther, P., Crozet, L., Jacome-Galarza, C.E., Händler, K., Klughammer, J., Kobayashi, Y., et al. (2016). Specification of tissue-resident macrophages during organogenesis. Science *353*, aaf4238. https://doi.org/10.1126/science.aaf4238.

50. Gomez Perdiguero, E., Klapproth, K., Schulz, C., Busch, K., Azzoni, E., Crozet, L., Garner, H., Trouillet, C., de Bruijn, M.F., Geissmann, F., and Rodewald, H.R. (2015). Tissue-resident macrophages originate from yolk-sac-derived erythro-myeloid progenitors. Nature *518*, 547–551. https://doi.org/10.1038/nature13989.

51. Croxford, A.L., Lanzinger, M., Hartmann, F.J., Schreiner, B., Mair, F., Pelczar, P., Clausen, B.E., Jung, S., Greter, M., and Becher, B. (2015). The Cytokine GM-CSF Drives the Inflammatory Signature of CCR2+ Monocytes and Licenses Autoimmunity. Immunity *43*, 502–514. https://doi.org/10.1016/j.immuni.2015.08.010.

52. Ginhoux, F., and Guilliams, M. (2016). Tissue-resident macrophage ontogeny and homeostasis. Immunity *44*, 439–449. https://doi.org/10.1016/j.immuni.2016.02.024.

53. Bain, C.C., Bravo-Blas, A., Scott, C.L., Perdiguero, E.G., Geissmann, F., Henri, S., Malissen, B., Osborne, L.C., Artis, D., and Mowat, A.M. (2014). Constant replenishment from circulating monocytes maintains the macrophage pool in the intestine of adult mice. Nat. Immunol. *15*, 929–937. https://doi.org/10.1038/ni.2967.

54. Gensollen, T., Lin, X., Zhang, T., Pyzik, M., See, P., Glickman, J.N., Ginhoux, F., Waldor, M., Salmi, M., Rantakari, P., and Blumberg, R.S. (2021). Embryonic macrophages function during early life to determine invariant natural killer T cell levels at barrier surfaces. Nat. Immunol. *22*, 699–710. https://doi.org/10.1038/s41590-021-00934-0.

55. Molawi, K., Wolf, Y., Kandalla, P.K., Favret, J., Hagemeyer, N., Frenzel, K., Pinto, A.R., Klapproth, K., Henri, S., Malissen, B., et al. (2014). Progressive replacement of embryo-derived cardiac macrophages with age. J. Exp. Med. *211*, 2151–2158. https://doi.org/10.1084/jem.20140639.

56. Liu, Z., Gu, Y., Chakarov, S., Bleriot, C., Kwok, I., Chen, X., Shin, A., Huang, W., Dress, R.J., Dutertre, C.A., et al. (2019). Fate Mapping via Ms4a3-Expression History Traces Monocyte-Derived Cells. Cell *178*, 1509–1525.e19. https://doi.org/10.1016/j.cell.2019.08.009.

57. Shaw, T.N., Houston, S.A., Wemyss, K., Bridgeman, H.M., Barbera, T.A., Zangerle-Murray, T., Strangward, P., Ridley, A.J.L., Wang, P., Tamoutounour, S., et al. (2018). Tissue-resident macrophages in the intestine are long lived and defined by Tim-4 and CD4 expression. J. Exp. Med. *215*, 1507–1518. https://doi.org/10.1084/jem.20180019.

58. Serbina, N.V., and Pamer, E.G. (2006). Monocyte emigration from bone marrow during bacterial infection requires signals mediated by chemokine receptor CCR2. Nat. Immunol. *7*, 311–317. https://doi.org/10.1038/ni1309.

59. Melmed, S., Kaiser, U.B., Lopes, M.B., Bertherat, J., Syro, L.V., Raverot, G., Reincke, M., Johannsson, G., Beckers, A., Fleseriu, M., et al. (2022). Clinical Biology of the Pituitary Adenoma. Endocr. Rev. *43*, 1003–1037. https://doi.org/10.1210/endrev/bnac010.

60. Hu, N., Gutsmann, A., Herbert, D.C., Bradley, A., Lee, W.H., and Lee, E.Y. (1994). Heterozygous Rb-1 delta 20/+mice are predisposed to tumors of the pituitary gland with a nearly complete penetrance. Oncogene *9*, 1021–1027.

61. Jacks, T., Fazeli, A., Schmitt, E.M., Bronson, R.T., Goodell, M.A., and Weinberg, R.A. (1992). Effects of an Rb mutation in the mouse. Nature *359*, 295–300. https://doi.org/10.1038/359295a0.

62. Abboud, D., Daly, A.F., Dupuis, N., Bahri, M.A., Inoue, A., Chevigné, A., Ectors, F., Plenevaux, A., Pirotte, B., Beckers, A., and Hanson, J. (2020). GPR101 drives growth hormone hypersecretion and gigantism in mice via constitutive activation of G(s) and G(q/11). Nat. Commun. *11*, 4752. https://doi.org/10.1038/s41467-020-18500-x.

63. Charles, M.A., Saunders, T.L., Wood, W.M., Owens, K., Parlow, A.F., Camper, S.A., Ridgway, E.C., and Gordon, D.F. (2006). Pituitary-Specific Gata2 Knockout: Effects on Gonadotrope and Thyrotrope Function. Mol. Endocrinol. *20*, 1366–1377. https://doi.org/10.1210/me.2005-0378.

64. Tremblay, J.J., and Drouin, J. (1999). Egr-1 is a downstream effector of GnRH and synergizes by direct interaction with Ptx1 and SF-1 to enhance luteinizing hormone beta gene transcription. Mol. Cell Biol. *19*, 2567–2576. https://doi.org/10.1128/MCB.19.4.2567.

65. Acampora, D., Mazan, S., Tuorto, F., Avantaggiato, V., Tremblay, J.J., Lazzaro, D., di Carlo, A., Mariano, A., Macchia, P.E., Corte, G., et al. (1998). Transient dwarfism and hypogonadism in mice lacking Otx1 reveal prepubescent stage-specific control of pituitary levels of GH, FSH and LH. Development *125*, 1229–1239. https://doi.org/10.1242/dev.125.7.1229.

66. Hodson, D.J., Romanò, N., Schaeffer, M., Fontanaud, P., Lafont, C., Fiordelisio, T., and Mollard, P. (2012). Coordination of calcium signals by pituitary endocrine cells in situ. Cell Calcium *51*, 222–230. https://doi.org/10.1016/j.ceca.2011.11.007.

67. Stojilkovic, S.S., Tabak, J., and Bertram, R. (2010). Ion channels and signaling in the pituitary gland. Endocr. Rev. *31*, 845–915. https://doi.org/10.1210/er.2010-0005.

68. Zhao, W., Zhang, Y., Ji, R., Knight, G.E., Burnstock, G., Yuan, H., and Xiang, Z. (2020). Expression of P2X receptors in the rat anterior pituitary. Purinergic Signal. *16*, 17–28. https://doi.org/10.1007/s11302-019-09685-y.

69. Yagasaki, Y., Katayama, Y., Kinoshita, Y., Nagata, T., Kawakami, Y., and Miyata, M. (2021). Macrophages are activated in the rat anterior pituitary under chronic inflammatory conditions. Neurosci. Lett. *748*, 135688. https://doi.org/10.1016/j.neulet.2021.135688.

70. Hoek, A., Allaerts, W., Leenen, P.J., Schoemaker, J., and Drexhage, H.A. (1997). Dendritic cells and macrophages in the pituitary and the gonads. Evidence for their role in the fine regulation of the reproductive endocrine response. Eur. J. Endocrinol. *136*, 8–24. https://doi.org/10.1530/eje.0.1360008.

71. Hoeffel, G., Chen, J., Lavin, Y., Low, D., Almeida, F.F., See, P., Beaudin, A.E., Lum, J., Low, I., Forsberg, E.C., et al. (2015). C-Myb(+) erythro-myeloid progenitor-derived fetal monocytes give rise to adult tissue-resident macrophages. Immunity *42*, 665–678. https://doi.org/10.1016/j.immuni.2015.03.011.

72. Epelman, S., Lavine, K.J., Beaudin, A.E., Sojka, D.K., Carrero, J.A., Calderon, B., Brija, T., Gautier, E.L., Ivanov, S., Satpathy, A.T., et al. (2014). Embryonic and adult-derived resident cardiac macrophages are maintained through distinct mechanisms at steady state and during inflammation. Immunity *40*, 91–104. https://doi.org/10.1016/j.immuni.2013.11.019.

73. Palis, J., and Yoder, M.C. (2001). Yolk-sac hematopoiesis: the first blood cells of mouse and man. Exp. Hematol. *29*, 927–936.

74. Sheng, J., Ruedl, C., and Karjalainen, K. (2015). Most Tissue-Resident Macrophages Except Microglia Are Derived from Fetal Hematopoietic Stem Cells. Immunity *43*, 382–393. https://doi.org/10.1016/j.immuni.2015.07.016.

75. Hoeffel, G., Wang, Y., Greter, M., See, P., Teo, P., Malleret, B., Leboeuf, M., Low, D., Oller, G., Almeida, F., et al. (2012). Adult Langerhans cells derive predominantly from embryonic fetal liver monocytes with a minor contribution of yolk sac–derived macrophages. J. Exp. Med. *209*, 1167–1181. https://doi.org/10.1084/jem.20120340.

76. Guilliams, M., De Kleer, I., Henri, S., Post, S., Vanhoutte, L., De Prijck, S., Deswarte, K., Malissen, B., Hammad, H., and Lambrecht, B.N. (2013). Alveolar macrophages develop from fetal monocytes that differentiate into long-lived cells in the first week of life via GM-CSF. J. Exp. Med. *210*, 1977–1992. https://doi.org/10.1084/jem.20131199.

77. Silvin, A., Qian, J., and Ginhoux, F. (2023). Brain macrophage development, diversity and dysregulation in health and disease. Cell. Mol. Immunol. *20*, 1277–1289. https://doi.org/10.1038/s41423-023-01053-6.

78. Yan, T., Wang, R., Yao, J., and Luo, M. (2023). Single-cell transcriptomic analysis reveals rich pituitary–Immune interactions under systemic inflammation. PLoS Biol. *21*, e3002403. https://doi.org/10.1371/journal.pbio.3002403.

79. Cazareth, J., Guyon, A., Heurteaux, C., Chabry, J., and Petit-Paitel, A. (2014). Molecular and cellular neuroinflammatory status of mouse brain after systemic lipopolysaccharide challenge: importance of CCR2/CCL2 signaling. J. Neuroinflammation *11*, 132. https://doi.org/10.1186/1742-2094-11-132.

80. Qian, B.Z., Li, J., Zhang, H., Kitamura, T., Zhang, J., Campion, L.R., Kaiser, E.A., Snyder, L.A., and Pollard, J.W. (2011). CCL2 recruits inflammatory monocytes to facilitate breast-tumour metastasis. Nature *475*, 222–225. https://doi.org/10.1038/nature10138.

81. Franklin, R.A., Liao, W., Sarkar, A., Kim, M.V., Bivona, M.R., Liu, K., Pamer, E.G., and Li, M.O. (2014). The cellular and molecular origin of tumor-associated macrophages. Science *344*, 921–925. https://doi.org/10.1126/science.1252510.

82. Bonnefont, X., Lacampagne, A., Sanchez-Hormigo, A., Fino, E., Creff, A., Mathieu, M.-N., Smallwood, S., Carmignac, D., Fontanaud, P., Travo, P., et al. (2005). Revealing the large-scale network organization of growth hormone-secreting cells. Proc. Natl. Acad. Sci. USA *102*, 16880–16885. https://doi.org/10.1073/pnas.0508202102.

83. Hodson, D.J., Schaeffer, M., Romanò, N., Fontanaud, P., Lafont, C., Birkenstock, J., Molino, F., Christian, H., Lockey, J., Carmignac, D., et al. (2012). Existence of long-lasting experience-dependent plasticity in endocrine cell networks. Nat. Commun. *3*, 605. https://doi.org/10.1038/ncomms1612.

84. Budry, L., Lafont, C., El Yandouzi, T., Chauvet, N., Conéjero, G., Drouin, J., and Mollard, P. (2011). Related pituitary cell lineages develop into interdigitated 3D cell networks. Proc. Natl. Acad. Sci. USA *108*, 12515–12520. https://doi.org/10.1073/pnas.1105929108.

85. Shipston, M.J. (2018). Control of anterior pituitary cell excitability by calcium-activated potassium channels. Mol. Cell. Endocrinol. *463*, 37–48. https://doi.org/10.1016/j.mce.2017.06.003.

86. Izumi, S.-I., Stojilković, S.S., and Catt, K.J. (1989). Calcium mobilization and influx during the biphasic cytosolic calcium and secretory responses in agonist-stimulated pituitary gonadotrophs. Arch. Biochem. Biophys. *275*, 410–428. https://doi.org/10.1016/0003-9861(89)90388-3.

87. Zemkova, H., Balik, A., Jiang, Y., Kretschmannova, K., and Stojilkovic, S.S. (2006). Roles of Purinergic P2X Receptors as Pacemaking Channels and Modulators of Calcium-Mobilizing Pathway in Pituitary Gonadotrophs. Mol. Endocrinol. *20*, 1423–1436. https://doi.org/10.1210/me.2005-0508.

88. Stojilkovic, S.S., He, M.-L., Koshimizu, T.a., Balik, A., and Zemkova, H. (2010). Signaling by purinergic receptors and channels in the pituitary gland. Mol. Cell. Endocrinol. *314*, 184–191. https://doi.org/10.1016/j.mce.2009.05.008.

89. Tomić, M., Jobin, R.M., Vergara, L.A., and Stojilkovic, S.S. (1996). Expression of Purinergic Receptor Channels and Their Role in Calcium Signaling and Hormone Release in Pituitary Gonadotrophs: INTEGRATION OF P2 CHANNELS IN PLASMA MEMBRANE-AND ENDOPLASMIC RETICULUM-DERIVED CALCIUM OSCILLATIONS. J. Biol. Chem. *271*, 21200–21208. https://doi.org/10.1074/jbc.271.35.21200.

90. Zumerle, S., Calì, B., Munari, F., Angioni, R., Di Virgilio, F., Molon, B., and Viola, A. (2019). Intercellular Calcium Signaling Induced by ATP Potentiates Macrophage Phagocytosis. Cell Rep. *27*, 1–10.e4. https://doi.org/10.1016/j.celrep.2019.03.011.

91. Zsembery, Á., Boyce, A.T., Liang, L., Peti-Peterdi, J., Bell, P.D., and Schwiebert, E.M. (2003). Sustained calcium entry through P2X nucleotide receptor channels in human airway epithelial cells. J. Biol. Chem. *278*, 13398–13408. https://doi.org/10.1074/jbc.M212277200.

92. Wang, C.M., Ploia, C., Anselmi, F., Sarukhan, A., and Viola, A. (2014). Adenosine triphosphate acts as a paracrine signaling molecule to reduce the motility of T cells. EMBO J. *33*, 1354–1364. https://doi.org/10.15252/embj.201386666.

93. Badimon, A., Strasburger, H.J., Ayata, P., Chen, X., Nair, A., Ikegami, A., Hwang, P., Chan, A.T., Graves, S.M., Uweru, J.O., et al. (2020). Negative feedback control of neuronal activity by microglia. Nature *586*, 417–423. https://doi.org/10.1038/s41586-020-2777-8.

94. Cserép, C., Pósfai, B., Lénárt, N., Fekete, R., László, Z.I., Lele, Z., Orsolits, B., Molnár, G., Heindl, S., Schwarcz, A.D., et al. (2020). Microglia monitor and protect neuronal function through specialized somatic purinergic junctions. Science *367*, 528–537.

95. McKinsey, G.L., Lizama, C.O., Keown-Lang, A.E., Niu, A., Santander, N., Larpthaveesarp, A., Chee, E., Gonzalez, F.F., and Arnold, T.D. (2020).

A new genetic strategy for targeting microglia in development and disease. Elife *9*, 545900–e54634. https://doi.org/10.7554/eLife.54590.

96. Macdonald, K.P.A., Palmer, J.S., Cronau, S., Seppanen, E., Olver, S., Raffelt, N.C., Kuns, R., Pettit, A.R., Clouston, A., Wainwright, B., et al. (2010). An antibody against the colony-stimulating factor 1 receptor depletes the resident subset of monocytes and tissue-and tumor-associated macrophages but does not inhibit inflammation. Blood *116*, 3955–3963. https://doi.org/10.1182/blood.

97. Rantakari, P., Auvinen, K., Jäppinen, N., Kapraali, M., Valtonen, J., Karikoski, M., Gerke, H., Iftakhar-E-Khuda, I., Keuschnigg, J., Umemoto, E., et al. (2015). The endothelial protein PLVAP in lymphatics controls the entry of lymphocytes and antigens into lymph nodes. Nat. Immunol. *16*, 386–396. https://doi.org/10.1038/ni.3101.

98. La Manno, G., Soldatov, R., Zeisel, A., Braun, E., Hochgerner, H., Petukhov, V., Lidschreiber, K., Kastriti, M.E., Lönnerberg, P., Furlan, A., et al. (2018). RNA velocity of single cells. Nature *560*, 494–498. https://doi.org/10.1038/s41586-018-0414-6.

99. Wolf, F.A., Angerer, P., and Theis, F.J. (2018). SCANPY: large-scale single-cell gene expression data analysis. Genome Biol. *19*, 15. https://doi.org/10.1186/s13059-017-1382-0.

100. Bergen, V., Lange, M., Peidli, S., Wolf, F.A., and Theis, F.J. (2020). Generalizing RNA velocity to transient cell states through dynamical modeling. Nat. Biotechnol. *38*, 1408–1414. https://doi.org/10.1038/s41587-020-0591-3.

101. Lange, M., Bergen, V., Klein, M., Setty, M., Reuter, B., Bakhti, M., Lickert, H., Ansari, M., Schniering, J., Schiller, H.B., et al. (2022). CellRank for directed single-cell fate mapping. Nat. Methods *19*, 159–170. https://doi.org/10.1038/s41592-021-01346-6.

102. Korsunsky, I., Millard, N., Fan, J., Slowikowski, K., Zhang, F., Wei, K., Baglaenko, Y., Brenner, M., Loh, P.R., and Raychaudhuri, S. (2019). Fast, sensitive and accurate integration of single-cell data with Harmony. Nat. Methods *16*, 1289–1296. https://doi.org/10.1038/s41592-019-0619-0.

103. McInnes, L., Healy, J., and Melville, J. (2020). UMAP: Uniform Manifold Approximation and Projection for Dimension Reduction. Preprint at ArXiv. https://doi.org/10.48550/arXiv.1802.03426.

104. Traag, V.A., Waltman, L., and van Eck, N.J. (2019). From Louvain to Leiden: guaranteeing well-connected communities. Sci. Rep. *9*, 5233. https://doi.org/10.1038/s41598-019-41695-z.

105. Lopez, R., Regier, J., Cole, M.B., Jordan, M.I., and Yosef, N. (2018). Deep generative modeling for single-cell transcriptomics. Nat. Methods *15*, 1053–1058. https://doi.org/10.1038/s41592-018-0229-2.

106. Boyeau, P., Regier, J., Gayoso, A., Jordan, M.I., Lopez, R., and Yosef, N. (2023). An empirical Bayes method for differential expression analysis of single cells with deep generative models. Proc. Natl. Acad. Sci. USA *120*, e2209124120. https://doi.org/10.1073/pnas.2209124120.

107. Kim, D., Paggi, J.M., Park, C., Bennett, C., and Salzberg, S.L. (2019). Graph-based genome alignment and genotyping with HISAT2 and HISAT-genotype. Nat. Biotechnol. *37*, 907–915. https://doi.org/10.1038/s41587-019-0201-4.

108. Pertea, M., Pertea, G.M., Antonescu, C.M., Chang, T.C., Mendell, J.T., and Salzberg, S.L. (2015). StringTie enables improved reconstruction of a transcriptome from RNA-seq reads. Nat. Biotechnol. *33*, 290–295. https://doi.org/10.1038/nbt.3122.

109. Liao, Y., Smyth, G.K., and Shi, W. (2014). FeatureCounts: An efficient general purpose program for assigning sequence reads to genomic features. Bioinformatics *30*, 923–930. https://doi.org/10.1093/bioinformatics/btt656.

110. R Development Core Team (2011). R: A Language and Environment for Statistical Computing, *1* (R Foundation for Statistical Computing). https://doi.org/10.1007/978-3-540-74686-7.

111. Gentleman, R.C., Carey, V.J., Bates, D.M., Bolstad, B., Dettling, M., Dudoit, S., Ellis, B., Gautier, L., Ge, Y., Gentry, J., et al. (2004). Bioconductor: open software development for computational biology and bioinformatics. Genome Biol. *5*, R80. https://doi.org/10.1186/gb-2004-5-10-r80.

112. Robinson, M.D., McCarthy, D.J., and Smyth, G.K. (2010). edgeR: A Bioconductor package for differential expression analysis of digital gene expression data. Bioinformatics *26*, 139–140. https://doi.org/10.1093/bioinformatics/btp616.

113. Zhang, Y., Parmigiani, G., and Johnson, W.E. (2020). ComBat-seq: batch effect adjustment for RNA-seq count data. NAR Genom. Bioinform. *2*, lqaa078. https://doi.org/10.1093/nargab/lqaa078.

114. Leek, J.T., Johnson, W.E., Parker, H.S., Jaffe, A.E., and Storey, J.D. (2012). The SVA package for removing batch effects and other unwanted variation in high-throughput experiments. Bioinformatics *28*, 882–883. https://doi.org/10.1093/bioinformatics/bts034.

115. Love, M.I., Huber, W., and Anders, S. (2014). Moderated estimation of fold change and dispersion for RNA-seq data with DESeq2. Genome Biol. *15*, 550. https://doi.org/10.1186/s13059-014-0550-8.

116. Subramanian, A., Tamayo, P., Mootha, V.K., Mukherjee, S., Ebert, B.L., Gillette, M.A., Paulovich, A., Pomeroy, S.L., Golub, T.R., Lander, E.S., and Mesirov, J.P. (2005). Gene set enrichment analysis: A knowledge-based approach for interpreting genome-wide expression profiles. Proc. Natl. Acad. Sci. USA *102*, 15545–15550. https://doi.org/10.1073/pnas.0506580102.

117. Liberzon, A., Subramanian, A., Pinchback, R., Thorvaldsdóttir, H., Tamayo, P., and Mesirov, J.P. (2011). Molecular signatures database (MSigDB) 3.0. Bioinformatics *27*, 1739–1740. https://doi.org/10.1093/bioinformatics/btr260.

118. Castanza, A.S., Recla, J.M., Eby, D., Thorvaldsdóttir, H., Bult, C.J., and Mesirov, J.P. (2023). Extending support for mouse data in the Molecular Signatures Database (MSigDB). Nat. Methods *20*, 1619–1620. https://doi.org/10.1038/s41592-023-02014-7.

119. Pfaffl, M.W. (2001). A new mathematical model for relative quantification in real-time RT-PCR. Nucleic Acids Res. *29*, e45. https://doi.org/10.1093/nar/29.9.e45.

120. Helenius, M., Jalkanen, S., and Yegutkin, G. (2012). Enzyme-coupled assays for simultaneous detection of nanomolar ATP, ADP, AMP, adenosine, inosine and pyrophosphate concentrations in extracellular fluids. Biochim. Biophys. Acta *1823*, 1967–1975. https://doi.org/10.1016/j.bbamcr.2012.08.001.

STAR★METHODS

KEY RESOURCES TABLE

REAGENT or RESOURCE	SOURCE	IDENTIFIER
Antibodies		
Anti-mouse CD3e-BV421 (145-2C11)	BD Biosciences	Cat# 562600; RRID:AB_11153670
Anti-mouse CD11b-BV786 (M1/70)	BD Biosciences	Cat# 740861; RRID: AB_2740514
Anti-mouse CD11b-BV510 (M1/70)	BioLegend	Cat# 101263; RRID: AB_2629529
Anti-mouse CD45-PerCP-Cy5,5 (30-F11)	BD Biosciences	Cat# 550994; RRID: AB_394003
Anti-mouse CD45-V450 (30-F11)	BD Biosciences	Cat# 560501; RRID: AB_1645275
Anti-mouse CD64-PE (X54-5/7.1)	BioLegend	Cat# 139304; RRID: AB_10612740
Anti-mouse CD64-BV786 (X54-5/7.1)	BD Biosciences	Cat#741024; RRID: AB_2740644
Anti-mouse CD115-Pe-Cy7 (AFS98)	eBioscience	Cat# 25-1152-80; RRID: AB_2573385
Anti-mouse CD163-A647 (S15049I)	BioLegend	Cat# 155302; RRID: AB_2734239
Anti-mouse/rat CD206-A488 (MR5D3)	Bio-Rad	Cat# MCA2235A488T; RRID: AB_2297790
Anti-mouse CD206-A647 (MR5D3)	BD Biosciences	Cat# 565250; RRID: AB_2739133
Anti-mouse CD206-BV650 (C068C2)	BioLegend	Cat# 141723; RRID: AB_2562445
Anti-mouse CX3CR1-BV650 (SA011F11)	BioLegend	Cat# 149033; RRID: AB_2565999
Anti-mouse CX3CR1-Pe-Cy7 (SA011F11)	BioLegend	Cat# 149015; RRID: AB_2565699
Anti-mouse F4/80-A488 (BM8)	eBioscience	Cat# 53-4801-82; RRID: AB_469915
Anti-mouse F4/80-BV510 (BM8)	Biolegend	Cat# 123135; RRID: AB_2562622
Anti-mouse F4/80-A647 (A3-1)	Bio-Rad	Cat# MCA497A647; RRID: AB_323931
Anti-mouse rat F4/80 (A3-1)	Bio X Cell	Cat# BE0206; RRID: AB_10949019
Anti-mouse rabbit P2Y12	AnaSpec	Cat# AS-55043A; RRID:AB_2298886
Anti-mouse P2RY12-A488 (S16007D)	BioLegend	Cat# 848015; RRID:AB_2936702
Anti-mouse P2RY12-PE (S16007D)	BioLegend	Cat# 848004; RRID:AB_2721644
Anti-mouse Panendothelial Cell Antigen-A488 (MECA-32)	BioLegend	Cat# 120506; RRID:AB_493305
Anti-KI67-A647 mouse (B56)	BD Biosciences	Cat# 561126; RRID:AB_10611874
Anti-mouse Ly6C-BV421 (AL-21)	BD Biosciences	Cat# 562727; RRID:AB_2737748
Anti-mouse Ly6C-A647 (Monts 1)	Elabscience	Cat# E-AB-F1121M
Anti-mouse I-A/I-E-A647 (M5/114.15.2)	BioLegend	Cat# 107618; RRID:AB_493525
Anti-mouse I-A/I-E-BV711 (M5/114.15.2)	BD Biosciences	Cat# 563414; RRID:AB_2738191
Anti-mouse SiglecF-PE-CF594 (E50-2440)	BD Biosciences	Cat# 562757; RRID:AB_2687994
Anti-mouse SiglecH (440c)	BD Biosciences	Cat# 747674; RRID:AB_2744235
Anti-mouse Lyve1-PE (223322)	R&D Systems	Cat# FAB2125P; RRID:AB_10889020
Anti-mouse Rabbit Lyve1	Relia Tech GmbH	Cat # 103-PA50; RRID:AB_2783787
RFP (tdTomato) Polyclonal Antibody Pre-adsorbed	Rockland	Cat# 600-401-379, RRID:AB_2209751
Anti-mouse rabbit LHb (AFP-C697071P)	A.F. Parlow National Hormone and Peptide Program	N/A
Anti-mouse/rat rabbit TSHb (AFP-1274789)	A.F. Parlow National Hormone and Peptide Program	N/A
Anti-mouse rabbit PRL (AFP-879151)	A.F. Parlow National Hormone and Peptide Program	N/A
InVivoMAb anti-mouse CSF1 (5A1)	Bio X Cell	Cat# BE0204; RRID: AB_10950309
InVivoMAb anti-mouse CSF1R (AFS98)	Bio X Cell	Cat# BE0213; RRID: AB_2687699
InVivoMAb rat IgG1 isotype control, anti-horseradish peroxidase (HRPN)	Bio X Cell	Cat# BE0088; RRID: AB_1107775

(*Continued on next page*)

Continued

REAGENT or RESOURCE	SOURCE	IDENTIFIER
InVivoMab rat IgG2a isotype control (2A3)	Bio X Cell	Cat# BE0089; RRID: AB_1107769
Rabbit anti-GNRHR Polyclonal antibody	Proteintech	Cat# 19950-1-AP; RRID:AB_10644155
Goat anti-Rabbit IgG (H + L) Highly Cross-Adsorbed Secondary Antibody, Alexa Fluor™ 488	Thermo Fisher Scientific	Cat# A-11034; RRID: AB_2576217
Goat Anti-Rabbit IgG (H + L) Highly Cross-adsorbed Antibody, Alexa Fluor™ 546	Invitrogen	Cat# A11035; RRID: AB_143051
Goat anti-Rat IgG (H + L) Cross-Adsorbed Secondary Antibody, Alexa Fluor™ 546	Invitrogen	Cat# A-11081; RRID: AB_2534125
Donkey anti-Rabbit IgG (H + L) Highly Cross-Adsorbed Secondary Antibody, Alexa Fluor™ Plus 647	Invitrogen	Cat# A32795; RRID: AB_2762835
Chemicals, peptides, and recombinant proteins		
50x TAE Electrophoresis Buffer	ThermoFisher Scientific	Cat# B49
Acetone	Merck	Cat# 1.00014.2500
ATP disodium salt hydrate	Sigma-Aldrich	Cat# A2383-1G
Benzyl alcohol	Honeywell	Cat# 402834-100ML
Benzyl benzoate	Sigma-Aldrich	Cat# B6630-250ML
Bovine Serum Albumin (BSA) Lyophilised pH ~7	BioWest	Cat# P615 -100GR
Collagenase D	Roche	Cat# 11088866001
DAPI (4′,6-Diamidino-2-Phenylindole, Dihydrochloride)	Invitrogen	Cat# D1306
DMSO (Dimethyl sulfoxide)	Sigma-Aldrich	Cat# D4540-100ML
DNase I	Roche	Cat# 10104159001
DPX Mountant for histology	Sigma-Aldrich	Cat# 06522
Dulbecco's Phosphate Buffered Saline	Sigma-Aldrich	Cat# D8537-500ML
Dulbecco's Modified Eagle Medium F12	Gibco	Cat# 11320033-500ML
Dulbecco's Modified Eagle Medium	Gibco	Cat# 31053028-500ML
Eosin Solution, 0.1%	Reagena	Cat# 180072
Ethanol	Altia Industrial	N/A
Fetal calf serum	Biowest	Cat#: S181B-500
Fixable Viability Dye eFluor 780	eBioscience	Cat# 65-0865-14
Formalin solution, neutral buffered, 10%	Sigma-Aldrich	cat# HT501128
GlutaMAX™ Supplement	Gibco	Cat#: 35050061
Hank's Balanced Salt Solution	Sigma-Aldrich	Cat# RNBF2378
Lipopolysaccharides from Escherichia coli O55:B5	Sigma-Aldrich	Cat# L4524-5MG
LHRH acetate salt	BACHEM	Cat# 4033013-25MG
Mayer's Hematoxylin Solution	Sigma-Aldrich	Cat# MHS16-500ML
Methanol, Certified AR for Analysis	Fisher Chemical	Cat# M/4000/PC17
Normal mouse serum	Jackson ImmunoResearch	Cat# 015-000-120
Normal goat serum	Jackson ImmunoResearch	Cat# 055-000-121
OCT Compound	Tissue-Tek	Cat# 4583
Paraformaldehyde solution 4% in PBS	Santa Cruz Biotechnology	Cat# sc-281692
Percoll	Cytiva	Cat# GE17-0891-02
Penicillin-Streptomycin 100x	Euroclone	Cat# ECB3001D
Progesterone	Sigma-Aldrich	Cat# P0130-25G
ProLong™ Gold Antifade Mountant without DAPI	Thermo Fisher Scientific	Cat# P36930

(*Continued on next page*)

Continued

REAGENT or RESOURCE	SOURCE	IDENTIFIER
Proteinase K	Macherey-Nagel	Cat# 740396
Standard Agarose-Type LE	BioNordika	Cat# BN-50004
Tamoxifen	Sigma-Aldrich	Cat# T5648-1G
Triton X-100	Sigma-Aldrich	Cat# T8787
UltraComp eBeads	eBioscience	Cat# 01-2222-42
Xylene	VWR Chemicals	Cat# 28973.363
Critical commercial assays		
Alexa Fluor 647 protein Labeling kit	Invitrogen	Cat# A20173
ATPlite 1step Luminescence Assay Kit	Revvity	Cat# 6016941
β-Gal Staining Kit	Invitrogen	Cat# K1465-01
Chromium Single Cell 3′ Library and Gel Bead Kit v2	10X Genomics	Cat# 120237
Mix2Seq kit	Eurofins	N/A
MyTaq Extract-PCR kit	Bioline	Cat# BIO-21117
MILLIPLEX MAP Mouse Pituitary Magnetic Bead Panel - Endocrine Multiplex Assay	Millipore	Cat# MPTMAG-49K
Mouse IL-6 Uncoated ELISA	Invitrogen	Cat# 88-7064
MyTaq HS Red Mix 2x	Bioline	Cat# BIO-25048
NucleoSpin DNA Rapid Lyse	Macherey-Nagel	Cat# 740100.250
NucleoSpin Tissue	Macherey-Nagel	Cat# 740952.50
RNeasy Plus Micro Kit	Qiagen	Cat# 74034
SensiFast^{Tm} cDNA Synthesis Kit	Bioline	Cat# BIO-65053
Deposited data		
ScRNA-seq raw and analyzed data	This paper	GEO: GSE284051
Bulk RNA-seq raw and analyzed data	This paper	GEO: GSE284384
Experimental models: Organisms/strains		
Mouse: C57BL/6NRj (6N)	Janvier Labs	https://janvier-labs.com/en/fiche_produit/c57bl-6nrj_mouse/; RRID:IMSR_RJ:C57BL-6NRJ
Mouse: B6.129S4-*Ccr2*^{tm1Ifc}/J (*Ccr2*$^{-/-}$)	The Jackson Laboratory	Stock# 004999; RRID: IMSR_JAX:004999
Mouse: B6.129P2(C)-*Cx3cr1*$^{tm2.1(cre/ERT2)Jung}$/J	The Jackson Laboratory	Stock# 020940 RRID: IMSR_JAX:02094
Mouse: B6.Cg-Gt(ROSA) 26Sortm14(CAG-tdTomato)Hze/J	The Jackson Laboratory	Stock# 007914; RRID: IMSR_JAX:007914
Mouse: B6.129X1-Gt(ROSA) 26Sor$^{tm1(EYFP)Cos}$/J (R26R-EYFP)	The Jackson Laboratory	Stock# 006148; RRID: IMSR_JAX:006148
Mouse: C57BL/6NTac-Ccr2tm2982 (T2A-Cre7ESR1-T2A-mKate2)BB	Prof. Burkhard Becher (University of Zurich)	N/A
Mouse: B6-Il34tm1.ec/bb (Il34LacZ)	Prof. Burkhard Becher (University of Zurich)	N/A
Mouse: Ms4a3tm1(cre/ERT2)Smoc	Prof. Florent Ginhoux (INSERM)	N/A
Mouse: Rb1tm1Tyj (B6.129S2-Rb1tm1Tyj)	Prof. Jorma Torppari (University of Turku)	N/A
Oligonucleotides		
qPCR primer sequences, see Method details for mRNA expression by quantitative real-time PCR	This paper	N/A

(*Continued on next page*)

Continued

REAGENT or RESOURCE	SOURCE	IDENTIFIER
Software and algorithms		
BioRender Illustration design tool	BioRender	https://www.biorender.com/; RRID:SCR_018361
CaseViewer	3D Histech	https://www.3dhistech.com/caseviewer; RRID:SCR_01765
CorelDRAW Graphics Suite X7 (64-bit), v16	Corel Corporation	https://www.coreldraw.com/en/; RRID: SCR_014235
BD FACSChorus™ Software 5.1.	BD Biosciences	https://www.bdbiosciences.com/en-us/products/software/instrument-software/bd-facschorus-software
BD FACSDiVa™ software version 8	BD Biosciences	http://www.bdbiosciences.com/us/instruments/clinical/software/flow-cytometry-acquisition/bd-facsdiva-software/m/333333/overview
FlowJo, version 10	FlowJo, Treestar Inc	https://www.flowjo.com/; RRID: SCR_008520
GraphPad Prism, v10.1.2	GraphPad Software	https://www.graphpad.com/scientific-software/prism/; RRID: SCR_002798
ImageJ, v1.51j8	National Institutes of Health	https://imagej.net/ImageJ; RRID: SCR_003070
Office (Word, Excel) Microsoft	Microsoft	https://www.microsoft.com
Python, ver. 3.10	Python Software Foundation	https://www.python.org/
R, R Development Core Team		https://www.r-project.org/
R Studio		https://www.rstudio.com/
Other		
35 mm Dish, No. 1.5 Coverslip, 14 mm Glass Diameter, Uncoated	MatTek Life Sciences	Cat# P35G-1.5-14-C
35 mm Dish, No. 1.5 Coverslip, 7 mm Glass Diameter, Uncoated	MatTek Life Sciences	Cat# P35G-1.5-7-C
SuperFrost Plus Adhesion slides Microscope Slides	Epredia	Cat# J1800AMNZ
Glass Square Coverslips 22 mm × 22 mm, No. 1	Fisherbrand	Cat# 12333128
Cover glass 24 mm × 60 mm, No. 1.5	Menzel-Gläser from VWR	Cat# 630-2108

EXPERIMENTAL MODEL AND STUDY PARTICIPANT DETAILS

Mice

Multiple genetic mouse models were used in this study: *Ccr2*$^{-/-}$ (stock 004999), *R26*^{EYFP} (stock 006148), *R26*^{tdTomato} (stock 007914), and *Cx3cr1*^{CreERT2} (stock 020940) were purchased from Jackson Laboratories. *CCR2*^{CreERT2} and *IL34*^{lac} mice were kindly provided by Prof. Dr. Burkhard Becker, *Ms4a3*^{CreERT2} mice were kindly provided by Prof. Florent Ginhoux, and *Rb1*^{tm1Tyj} mice were kindly provided by Prof. Jorma Toppari. Wild-type (WT) mice, C57BL/6N, were acquired from Janvier labs. Experiments with 1-week and older were performed only with male mice. In embryonic and NB timepoints the whole litter was pooled for pituitary gland samples. All experimental mice were kept in specific pathogen-free conditions and under controlled environmental conditions at a temperature of 21°C ± 3°C, humidity 55% ± 15%, and 12/12 h light cycle at the Central Animal Laboratory of the University of Turku (Turku, Finland). Mice had food and water *ad libitum*. Animal experiments were conducted under the revision and approval of the Regional Animal Experiment Board in Finland, according to the 3R principle, and under Animal license numbers 6211/04.10.07/2017 and 14685/2020. All experiments were regulated according to the Finnish Act on Animal Experimentation (497/2013). Embryonic development was estimated considering the day of a vaginal plug as embryonic day 0.5 (E0.5).

Primary cell culture

Pituitary glands from 8-week-old WT male mice were collected, and cells were isolated according to the single-cell isolation protocol described below. The pituitaries from 8 to 18 mice were pooled in all experiments. Pituitary macrophages and gonadotrophs (live/CD45$^-$/GNRHR$^+$) were sorted in Dulbecco's Modified Eagle Medium (DMEM) with 10% Fetal Calf Serum (FCS) using BD FACSDiscover S8 Cell Sorter (100-μm nozzle, Becton Dickinson). The purity of the isolated populations was >95%. Sorted cells were seeded 96-well plates (5000–6000 cells/well of macrophages or gonadotrophs alone and 10,000 to 12,000 cells/well in co-cultures) in Dulbecco's Modified Eagle's Medium/Nutrient Mixture F12 (DMEM/F12) medium with 10% fetal calf serum, 1 X GlutaMAX, 100 IU/mL penicillin and 100 μg/mL streptomycin. All cells were cultured at 37°C in a humidified atmosphere containing 5% CO2, and experiments were performed after 24 h or 48 h of culture.

METHOD DETAILS

In all experiments, the pituitary gland and other samples were collected between 8 a.m. and 9:30 a.m.

Single-cell isolation

The pregnant females were euthanized by carbon dioxide (CO_2) asphyxiation followed by cervical dislocation. Embryos were dissected from the uterus and euthanized through decapitation. Newborn and 7-day-old pups were euthanized by decapitation. From 2 weeks of age onwards, euthanasia was carried out using CO2 asphyxiation followed by cervical dislocation or cardiac puncture. For the scRNA sequencing, 3- and 8-week-old male mice were sacrificed with CO_2, the chest cavity was opened by two parasternal incisions, and the perfusion was started immediately. The perfusion was done through the left ventricle using a peristaltic pump (Harvard peristaltic Pump P-230, Harvard apparatus) with a constant pressure of 5 mL/min for 3 min with cold PBS. The right atrium was opened for the outflow. The skull was carefully opened, and the brain was removed to expose the pituitary gland, which was then collected as a whole. For scRNA sequencing and flow cytometry, whole pituitaries or separate posterior and anterior pituitaries were mechanically lysed by suspending and digested with 50 μg/mL DNase 1 (Roche) and 1 mg/mL Collagenase D (Roche) in Hank's Buffered Saline (HBSS; Sigma-Aldrich) at 37°C for 30–45 min. The cell suspension was filtered through silk (pore size 77 μm), pelleted (1006G, 1.5 min), and washed with 500 μL of HBSS to remove enzymes. Finally, cells were eluted to Phosphate Buffered Saline (PBS; Sigma-Aldrich) before labeling for cell sorting or analyzing flow cytometry.

Blood from mouse embryos to 1 week of age mice was collected by bleeding the body to heparin-PBS (50 μL of 100 IU/mL heparin in 500 μL of PBS). From 2 weeks of age onwards, blood was drawn by cardiac puncture into heparinized syringes, and erythrocytes were lysed from the blood as described.[97]

Brain, liver, and lungs were carefully dissected, minced with scissors, and digested with 50 μg/mL Dnase 1 and 1 mg/ml Collagenase D in HBSS at 37°C (20 min for brain and 60 min for liver and lung) and then passed through a 70-μm cell strainer. The brain cells were then resuspended in isotonic Percoll (Sigma-Aldrich), and the microglia were isolated as described.[46] Finally, cells were eluted to PBS before labeling for flow cytometry.

ScRNA sequencing and data analysis

Single-cell suspensions derived from WT pituitary glands at NB, 1, 3, and 8 weeks of age were stained with Fixable Viability Dye eFluor 780 (eBioscience) to label the dead cells (Pooled samples of NB n = 31, 1 week n = 15, 3 weeks n = 25 and 8 week n = 21 animals). Unspecific binding to low-affinity Fc-receptors was blocked by incubating the cells with unconjugated CD16/32 antibody (BioXCell, clone 2.4G2). Cells were subsequently stained for 30 min at 4°C with antibodies diluted to the FACS buffer. The cells were sorted with Sony SH800 Cell Sorter (Sony Biotechnology Inc.). Single cells were gated with the FSC-H versus FCS-W plot and the SSC-H versus SSC-W plot to avoid doublets and dead cells were excluded. Live single CD45$^+$ cells were sorted into the RPMI medium containing 2% FCS.

Freshly sorted CD45$^+$ were processed immediately according to 10X Genomics guidelines (CG000126_Guidelines for Optimal Sample Prep Flow Chart RevA). Single-cell RNA-sequencing libraries were prepared according to the manufacturer's instructions (CG00052 RevB) using Chromium Single Cell 3′ Library and Gel Bead Kit v2 (10X Genomics, 120237) and Chromium Single Cell A Chip Kit (10X Genomics). Prepared libraries were sequenced using the Illumina Novaseq6000 Sequencing System (RRID: SCR_016387). The library preparation was executed at the Single Cell Omics core, and the sequencing was conducted at the Finnish Functional Genomics Center, both housed within Turku Bioscience Center, Finland.

The *Cell Ranger* (ver. 7.1.0) "count" function was used to align samples to the *mm10-2020-A* reference genome, quantify reads, and filter reads and barcodes. Spliced/unspliced counts for RNA velocity estimation were calculated with the Python implementation of *Velocyto* (ver. 0.17.17, SCR_018167[98]). Data analysis and displays were generated using the *scanpy* (ver. 1.9.8, SCR_018139[99]), *scVelo* (ver. 0.3.1, SCR_018168[100]), *CellRank* (ver. dev2.0.2, SCR_022827[101]), and Python (ver. 3.10, SCR_008394) toolboxes.

For quality control, low-quality cells were filtered out in each sample by the number of expressed unique genes and percentage of mitochondrial genes (max.: 8%). Genes with less than 20 shared spliced/unspliced counts and genes expressed by fewer than 3 cells were removed. Counts per cell were normalized as total counts over all genes (*target sum: 10^4*) and were log1p transformed. Principal components (PCA) were calculated and used for sample integration with harmony (ver. 0.0.6[102]). For the complete dataset, the neighborhood graph (nearest neighbors: 50), Uniform Manifold Approximation and Projection (UMAP; SCR_018217[103]; min.

distance: 0.5, neg. edge sample rate: 8), and Leiden clustering (ver. 0.9.1[104]; resolution: 1.8) were computed with the indicated settings.

Clusters containing monocytes and macrophages were selected by marker gene expression, and neighborhood graph (*nearest neighbors: 50*), UMAP (*min. distance: 0.7, neg. edge sample rate: 12*), and Leiden clustering (*resolution: 0.75*) were re-computed. Transcriptional dynamics were re-constructed using scVelo's generalized dynamical model, and CellRank's CytoTRACE Kernel (*threshold scheme: soft*) was used to derive a pseudotime ordering of cells based on cellular plasticity estimation. Differential expression genes were computed with sci-tools's (ver. 1.0.4) single cell Variational Inference (scVI; *layer: counts, categorical covariates: batch, continuous covariate: pct_counts_mt*) model[105] and the *differential_expression* function (*mode: "change', delta: 0.25, fdr_target: 0.05*;[106]).

In utero and adult tamoxifen administration

Cx3cr1^{CreERT2} and *CCR2*^{CreERT2} mice were crossed with *R26*^{EYFP} or *R26*^{tdTomato} reporter mice to study embryonic-derived macrophages. To study bone marrow-derived macrophages, *Ms4a3*^{CreERT2} mice were crossed with the *R26*^{tdTomato} reporter strain. For *in utero* tamoxifen induction of CRE activity, a single dose of tamoxifen (1.5 mg/dam, mended with 0.75 mg progesterone; Sigma–Aldrich) was administered i.p. to pregnant females on indicated pregnancy days. For adult tamoxifen induction, *Cx3cr1*^{CreERT2}*; R26*^{EYFP} or *Ms4a3*^{CreERT2}*; Rosa*^{tdTomato} mice were administered i.p. 5 consecutive days of tamoxifen (75 mg tamoxifen/kg). This induction scheme leads to selective labeling of CX3CR1 positive macrophages and monocytes or bone marrow-derived monocytes.

Flow cytometry

Cells were stained with Fixable Viability Dye eFluor 780 (eBioscience) to label the dead cells. Unspecific binding to low-affinity Fc-receptors was blocked by incubating the cells with unconjugated CD16/32 antibody (BioXCell, clone 2.4G2). Cells were subsequently stained for 30 min at 4°C with antibodies diluted to the FACS buffer, washed, and fixed with 1% formaldehyde in PBS. Samples were acquired with LSRFortessa flow cytometer with FACSDiVaTM version 9.0 software (Becton Dickinson), and data were analyzed using FlowJo v10.8 Software (BD Life Sciences).

Immunofluorescence staining and confocal microscopy

For whole-mount stainings, pituitary glands were collected from male mice at 17.5, newborn, 1 week, 2 weeks, 5 weeks, and 8 weeks of age. Pituitaries were dissected attached to the skull to prevent the gland from breaking. Samples were prepared for whole-mount staining by fixing them in 2% paraformaldehyde (PFA, Santa Cruz Biotechnology) in PBS for 20 min on ice. Samples were washed in PBS (3 × 10 min) shaking. The pituitaries were dissected from the skull between the second and third wash. Whole-mount samples were dehydrated in a graded methanol series and stored at −20°C. Samples were rehydrated through ascending series of methanol and finally placed into PBS. In brief, samples were blocked [1% normal goat serum (NGS) + 0.5% fetal calf serum (FCS) + 1% bovine serum albumin (BSA) + 0.4% Triton X-100 in PBS] and then sequentially incubated with primary unconjugated antibodies, secondary antibodies and directly conjugated antibodies diluted in blocking solution. Finally, the samples were dehydrated with increasing methanol series and subsequently optically cleared in glass-bottom microwell dishes first with 50% benzyl alcohol (Honeywell) 1:2 benzyl benzoate (BABB; Sigma–Aldrich) in methanol and then with 100% BABB, which was also used as a mounting medium.

For immunofluorescence stainings, pituitaries were embedded in OCT medium (Tissue-Tek), freezed on dry ice, and stored at −80°C prior to cryosectioning. Pituitaries were cut into 5-7-μm-thick sections and fixed with ice-cold acetone for 5 min. Before staining, samples were post-fixed in 2% PFA for 15 min at room temperature (RT) and rinsed in PBS. Samples were blocked for 1 h at RT in a humidity chamber in a blocking buffer (1% FCS, 1% NMS, and 5% NGS in 0.3% Triton X-PBS). Primary antibodies used for LHβ (1:1000, anti-mouse rabbit, Parlow), TSH (1:1000, Parlow), or PRL (1:1000, Parlow) were diluted in blocking solution and applied to sections overnight at 4°C. Sections were then washed 2 times 3 min in 0.1% TritonX-PBS. After washes, a fluorescent secondary antibody was added for 60 min at RT, followed by washes in 0.1% TritonX-PBS for 3 times 5 min and a rinse in PBS. Sections were counterstained with DAPI (1:5000 in PBS, 25 μL per section) and incubated for 10 min in a humidity chamber at RT. Sections were rinsed in PBS and MQ water. Finally, slides were mounted with the Mounting Prolong Gold antifade without DAPI (ThermoFisher Scientific).

Imaging was performed using an LSM880 confocal microscope (Zeiss) with an Axio Observer.Z1 microscope using ZEN 2.3 SP1 black edition acquisition software at RT. The objectives used were a Zeiss Plan-Apochromat 10×/0.45 without immersion, Zeiss Plan-Apochromat 20x/0.8 without immersion, Zeiss LD LCI Plan-Apochromat 25x/0.8 with glycerol immersion, and Zeiss LD LCI Plan-Apochromat 40x/1.2 with water immersion. Background subtractions, linear brightness and contrast adjustments were performed with ImageJ software (National Institute of Health).

X-gal staining

For X-gal staining, 5-week-old male mice were sacrificed with CO_2, the chest cavity was opened by two parasternal incisions, and the perfusion was started immediately. Mice were perfused first with 10 mL of PBS and then with 10 mL of 2% PFA in PBS. The right atrium was opened for the outflow. After collection, the pituitaries were fixed in 2% formaldehyde and 0.2% in PBS solution for 15 min. After fixation, the pituitary glands were embedded into OCT blocks and frozen at −80°C. Pituitaries were cut into 6 μm

sections with cryotome and fixed in acetone for 5 min. Staining was done with a β-gal staining kit (Invitrogen), according to the manufacturer's instructions, with the X-gal dissolved in DMSO (Sigma-Aldrich). Exceptions were that slides were washed 3 times with PBS after fixation, and after staining, washing was done with 1 x PBS and water. Slides were dehydrated with 96% ethanol for 30 s. Counterstaining was done with 0.1% eosin solution (180072, Reagena) for 3 min, after which slides were dehydrated in ethanol and xylene series. Mounting was done with DPX mountant for histology (Sigma-Aldrich). Slides were imaged with Pannoramic P1000 (3DHISTECH) and analyzed with Pannoramic Viewer (Version 1.15.4, 3DHISTECH).

LPS treatment

A single injection of Lipopolysaccharides (LPS) from *Escherichia coli* (O55:B5; Merck; 20 μg) was given i.p. for adult 8–10 weeks old WT or 9–10 weeks old *Ms4a3*^{CreERT2}*; R26*^{tdTomato} male mice. Control mice were injected with the same volume of PBS. The pituitary glands were analyzed by flow cytometry 24 h later. For treatment control, blood was collected from the treated mice by cardiac puncture, and serum was separated by centrifugation. IL-6 was analyzed from blood serums by sandwich enzyme-linked immunosorbent assay (ELISA; Thermo Fisher Scientific) according to the manufacturer's instructions.

Antibody treatment experiments

To specifically target yolk sac-derived macrophages in the offspring, pregnant C57BL/6N females at embryonic day 6.5 (E6.5) were treated with a single intraperitoneal (i.p.) injection of a function-blocking antibody against CSF1R (AFS98; Bio X Cell) or received rat IgG2a control antibody (clone 2A3; Bio X Cell). Each injection consisted of 3 mg of the respective antibody dissolved in sterile PBS. The pituitary glands, testis, and brains were collected at E17.5 for flow cytometric analyses.

A single injection of neutralizing CSF1 antibody (5A1; Bio X Cell; 150 μg), preventing the binding to CSF1R, or a function-blocking antibody to CSF1R (150 μg) was given i.p. for newborn mice. Control mice were injected with control IgG (HRPN; Bio X Cell; 150 μg) or rat IgG2a control antibody (2A3; Bio X Cell; 150 μg). The pituitary glands were analyzed by flow cytometry 48 h later. The brain was used as treatment control tissue.

To address the functional importance of macrophages for normal pituitary gland function, we ablated the pre-existing tissue-resident macrophages with CSF1R and gave the first injection during embryo development at E6.5. In a long depletion experiment, CSF1R was additionally given on postnatal day (P) 2, P14, and 4 weeks of age (4 times in total). The pituitary glands and brains were collected at 5 weeks of age.

Histological analyses

Pituitary glands were dissected attached to the skull and fixed with 10% Formalin (Sigma-Aldrich) at RT overnight. After fixing, pituitary glands were dehydrated through graded ethanol (EtOH) series at RT. 5 μm thick sections were cut and stained with Mayers hematoxylin (Sigma-Aldrich) and eosin (Reagena). Slides were mounted with DPX mountant for histology (Sigma-Aldrich), imaged with Pannoramic P1000 (3DHISTECH), and analyzed with Pannoramic Viewer (Version 1.15.4, 3DHISTECH).

Bulk RNA sequencing and data analysis

To determine the gene expression signature of macrophage-depleted pituitaries, we performed bulk RNA-seq from the total RNA of the pituitary glands collected after long CSF1R antibody treatment (see protocol above). RNA was isolated with RNeasy Plus Micro Kit (Qiagen) according to the manufacturer's protocol and analyzed on Advanced Analytical Fragment Analyzer for quality assessment. The sequencing run was performed using Illumina NovaSeq 6000 SP v1.5 (650–800 M reads/run, 2 lanes; Illumina) in the Finnish Functional Genome Center (Turku Bioscience Center, Finland). The quality of the sequenced reads was investigated. The reads were aligned to the mouse reference genome (GRCm38 release 94) using HISAT2 v2.0.5.[107] The novel gene assembly was predicted using StringTie v1.3.3b[108] using the mapping information from all the samples and the novel gene annotation was performed using Pfam, Swissprot, Go, and KEGG. The number of uniquely mapped reads associated with each gene was counted using the featureCounts v1.5.0-p3[109] tool using Ensembl annotations. The downstream analysis of gene counts was performed using R v4.1.2[110] and corresponding Bioconductor v3.14.[111] The lowly expressed genes were filtered out by using filterByExpr in edgeR package.[112] To tackle the issue of batch effects, we corrected the gene counts using ComBat_seq function[113] in the SVA R package[114] which is specially designed for RNA-seq data. It corrects for the batch effect by fitting a negative binomial regression model. The batch-corrected counts were normalized for library size and statistically tested using the DESeq2 package.[115] The genes were considered differentially expressed if their adjusted *p* value, estimated using the Benjamini-Hochberg test was equal to or lower than 0.1 and absolute fold change was greater than or equal to 2 between the group comparison between IgG2a and CSF1R. Gene set enrichment analyses (GSEA) were performed using the GSEA v 4.3.3 (Broad Institute, Cambridge, MA) with the M5; GO: BP (containing 7796 gene sets) and M2; CP; REACTOME (containing 1261 gene sets) collections from the molecular signature database (https://www.gsea-msigdb.org/gsea/msigdb/index.jsp). Analysis was performed in January 2024, with a significant p value < 0.05 and a false discovery rate (FDR) < 0.25.[116–118] In addition, ingenuity pathway analysis (IPA) was performed using IPA software (Qiagen, CA, USA). IPA analysis was performed using DE genes with a significant p value < 0.05 and fold change >1.6.

Hormone measurements

Concentrations of ACTH, LH, FSH, GH, TSH, and PRL, or LH alone were analyzed from homogenized pituitary glands, serum samples or culture medium in a single run on a Luminex 200 platform using a MILLIPLEX MAP Mouse Pituitary Magnetic Bead Panel (Millipore) according to the manufacturer's instructions. For the intrapituitary hormone measurements, pituitaries were dissected in the morning and homogenized in 500 μL phosphate-buffered saline (PBS). For serum hormone measurements, blood was collected from the mice in the morning by cardiac puncture, and serum was separated by centrifugation. For medium samples, cell culture medium was collected from *in vitro* experiments of sorted gonadotrophs and gonadotroph-pitMØ co-cultures. Intra- and inter-assay coefficients of variation (CV) were lower than 12.4%. The lowest detection limits for intrapituitary ACTH, LH, FSH, GH, TSH, and PRL measurements were 1.7, 4.9, 9.5, 1.7, 1.9, and 46.2 pg/mL, respectively.

mRNA expression by quantitative real-time PCR

Tissues were snap-frozen with liquid nitrogen, and total RNA was extracted. DNAse treatment was carried out with RNeasy Plus Micro/Mini Kit (Qiagen) following the manufacturer's instructions. RNA samples were dissolved in water, and after the quality check, RNA was used for cDNA synthesis using a SensiFast cDNA synthesis kit (Bioline). qPCR reactions were performed with TaqMan Universal Master Mix II (Applied Biosystems). Gene expression was quantified by QuantStudio 3 or 12K Flex Real-Time PCR Systems (Thermo Fisher Scientific). The mRNA expression of *Gnrhr* was normalized to the expression of *Actb*, and the expression of mRNA was quantified using the PfaffI method.[119] The sequences of the primers used for *Gnrhr* were 5′-TGCTCGGCCATCAACAACA-3′ and 5′-GGCAGTAGAGAGTAGGAAAAGGA-3′, and for *Actb*, 5′-CGTGGGCCGCCCTAGGCACCA-3′ and 5′-TTGGCCTTAGGGTTCAGGGGG-3′. The expression of *Gnrhr* was analyzed in the pituitary glands of CSF1R- and IgG control-treated mice (n = 4).

In vitro ATP measurements

After the one-day culture, the medium was changed to fresh DMEM/10% FCS only. To avoid undesirable ATP hydrolysis by serum-soluble nucleotidases, FCS was additionally heat-inactivated for 5 min at 60°C. The cells were allowed to rest for 30 min at 37°C. After a resting period, 100 μL aliquot of the medium was carefully collected from the top of the wells for basal extracellular ATP measurements. Extracellular ATP was measured also after stimulation with 10 μM GnRH (LHRH, Bachem) for 3h. ATP concentration was determined using bioluminescent enzyme-coupled assay[120] with ATPlite 1step Luminescence Assay Kit (Revvity). All measurements were performed using the Tecan Infinite M200 microplate reader (Salzburg, Austria). Calibration curves were generated for each experiment.

In vitro LH determination

After 24 h or 48 h of culture, the medium was replaced with fresh DMEM containing 10% FCS without antibiotics. To stimulate LH production and secretion, some wells were supplemented with 10 μM GnRH (LHRH, Bachem). In certain experiments, a combination of 10 μM GnRH and 1 μM ATP was added. The cells were then incubated at 37°C for 3 h. After the incubation period, the medium was collected and centrifuged at 3000 rpm to remove cell debris. The resulting supernatant was stored at −20°C until the LH concentration was analyzed.

QUANTIFICATION AND STATISTICAL ANALYSIS

Statistical analyses

Adult mice were assigned to experimental groups without employing specific randomization methods, as comparisons involved mice with varying genetic backgrounds. The researchers conducted the experimental procedure while blinded to the genotype of the embryos. Statistical analyses were conducted using GraphPad Prism software version v10.1.2 (GraphPad Software Inc). All data are presented as mean values ± SEM. Comparisons between the time points, genotypes, or treatment groups were made using the nonparametric two-tailed Mann-Whitney test, parametric two-tailed t test, and one-way ANOVA test with Bonferroni post-hoc test. P-values lower than 0.05 were considered statistically significant. The value of each n can be found in the Figure legends.